

Atmospheric wind profiling based on LEO-LEO infrared-laser occultation

Andreas Plach

February 2014

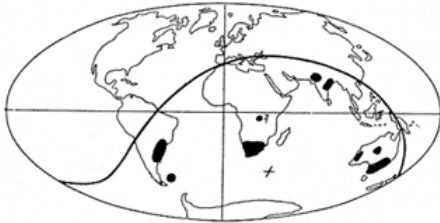


Financially supported by



The **Wegener Center for Climate and Global Change** combines as an interdisciplinary, internationally oriented research institute the competences of the University of Graz in the research area “Climate, Environmental and Global Change”. It brings together, in a dedicated building close to the University central campus, research teams and scientists from fields such as geo- and climate physics, meteorology, economics, geography, and regional sciences. At the same time close links exist and are further developed with many cooperation partners, both nationally and internationally. The research interests extend from monitoring, analysis, modeling and prediction of climate and environmental change via climate impact research to the analysis of the human dimensions of these changes, i.e., the role of humans in causing and being effected by climate and environmental change as well as in adaptation and mitigation. (more information at www.wegcenter.at)

The present report is the result of a Master thesis work completed in November 2013. The work was funded by the European Space Agency (ESA) under ESA-ESTEC Contract No. 4000105679/12/NL/CBi (AEXPWIND project).



Alfred Wegener (1880-1930), after whom the Wegener Center is named, was founding holder of the University of Graz Geophysics Chair (1924-1930). In his work in the fields of geophysics, meteorology, and climatology he was a brilliant scientist and scholar, thinking and acting in an interdisciplinary way, far ahead of his time with this style. The way of his ground-breaking research on continental drift is a shining role model—his sketch on the relations of continents based on traces of an ice age about 300 million years ago (left) as basis for the Wegener Center Logo is thus a continuous encouragement to explore equally innovative ways: *paths emerge in that we walk them* (Motto of the Wegener Center).

Wegener Center Verlag • Graz, Austria

© 2014 All Rights Reserved.

Selected use of individual figures, tables or parts of text is permitted for non-commercial purposes, provided this report is correctly and clearly cited as the source. Publisher contact for any interests beyond such use: wegcenter@uni-graz.at.

ISBN 978-3-9503608-4-4

February 2014

Contact: Mag. Andreas Plach, MSc.
andreas.plach@uni-graz.at

Wegener Center for Climate and Global Change
University of Graz
Brandhofgasse 5
A-8010 Graz, Austria
www.wegcenter.at

Masterarbeit
zur Erlangung des akademischen Grades eines
Master of Science
an der Karl-Franzens-Universität Graz

Atmospheric wind profiling based on LEO-LEO infrared-laser occultation

Andreas Plach

Betreuer: Univ.-Prof. Mag. Dr.rer.nat. Gottfried Kirchengast

Mitbetreuerin: Dipl.-Ing. Veronika Proschek

Wegener Center für Klima und Globalen Wandel
Universität Graz



Abstract

The present thesis uses the Low Earth Orbit (LEO) mission concept of LEO–LEO Microwave and Infrared-laser Occultation (LMIO). Its goal is the climate benchmark profiling of Greenhouse Gases (GHGs), thermodynamic variables and line-of-sight (l.o.s.) wind from space with focus on the Upper Troposphere–Lower Stratosphere (UTLS) region (5 km to 35 km) as an independent, self-calibrating, and active remote limb-sounding measurement concept.

So far only a so called *simple wind retrieval* algorithm, which assumes a constant wind velocity over the entire occultation ray path, was investigated. Here the implementation and results of a *new and advanced wind retrieval* algorithm are shown. It uses the more accurate assumption that the wind velocity is spherically symmetric within the UTLS. Therefore the wind can be retrieved by using an *Abel Transform*. The differential transmission principle is applied to two wind-sensitive absorption channels to minimize atmospheric *broadband effects*. The measured frequency shifts are proportional to the *wind-induced Doppler shift*.

The performance of the new algorithm is examined with end-to-end simulations. Synthetic and realistic l.o.s. wind profiles in three greatly different geographic regions are investigated. Furthermore two sets of satellite orbits, polar and near-polar, are analyzed.

The results show that the new wind retrieval is capable of deriving the l.o.s. wind speed in an approximate altitude range from 15 to 35 km, where it also works for highly variable wind profiles and high speed winds.

In a next step the frequency shift information will be used to correct the received GHG-sensitive infrared-laser signals for the wind-induced Doppler shift. This will lead to a more accurate GHG retrieval in windy air.

Zusammenfassung

Die vorliegende Arbeit nutzt das Low Earth Orbit (LEO) Missionskonzept der LEO-LEO Microwave and Infrared-laser Occultation (LMIO). Sein Ziel ist die Gewinnung von Profilen für Treibhausgase (THG), thermodynamische Zustandsvariablen und line-of-sight (l.o.s.) Wind von Satelliten aus, als unabhängiges, selbstkalibrierendes und aktives Limb-Sounding Messkonzept. Dabei liegt der Fokus auf der oberen Troposphäre und der unteren Stratosphäre (UTLS) (5 km bis 35 km).

Bisher wurde nur ein *einfacher Wind-Retrieval* Algorithmus untersucht. Dieser benutzt die Annahme einer konstanten Windgeschwindigkeit entlang des gesamten Okkultations-Strahlweges. Hier werden die Implementierung und die Ergebnisse für einen *neuen und fortgeschrittenen Wind-Retrieval* Algorithmus diskutiert. Dieser verwendet die genauere Annahme, dass die Windgeschwindigkeit in der UTLS sphärisch symmetrisch ist, daher kann der Wind über eine Abel-Transformation gewonnen werden. Das Differenzielle Transmissionsprinzip wird auf zwei Wind-Absorptionslinien angewandt, um atmosphärische *Breitband-Effekte* zu minimieren. Die gemessenen Frequenzverschiebungen sind proportional zur windinduzierten Dopplerverschiebung.

Die Leistungsfähigkeit des neuen Retrievals wird im Zuge von End-to-end Simulationen für synthetische und realistische l.o.s. Windprofile in drei stark unterschiedlichen geographischen Regionen untersucht. Außerdem werden zwei Sätze von Satellitenorbits, polar und polnahe Orbits, analysiert.

Die Ergebnisse zeigen, dass das neue Wind-Retrieval die Fähigkeit hat die l.o.s. Windgeschwindigkeit in einem Höhenbereich von etwa 15 bis 35 km abzuleiten, wobei es auch mit hochvariablen Windprofilen und hohen Windgeschwindigkeiten funktioniert.

In einem nächsten Schritt wird die beobachtete Frequenzverschiebung genutzt werden, um die THG-sensitiven Lasersignale um die windinduzierte Dopplerverschiebung zu korrigieren. Dies wird zu einem genaueren THG-Retrieval beitragen.

Acknowledgments

First and foremost, I would like to thank my advisor, Gottfried Kirchengast, for the opportunity to write my master thesis at the Wegener Center for Climate and Global Change, his valuable advice and assistance he offered in our meetings and in reviewing this thesis, the financial support he provided, and also for the chance to participate in my first international scientific workshop.

Furthermore, I would not have been able to finish my thesis as fast as I did, without the help of Veronika Proschek. Her troubleshooting skills concerning programming issues, her patience during the last months, and the review of this thesis are highly appreciated. I would wish every master student to have such a competent and helpful co-advisor.

Another grateful thanks goes out to my office roommates Thomas Berger, Lukas Brunner, Raimund Klingler, and Jakob Schwarz for their helpful advice and support. They made our office a great working environment and we also had one or the other laugh.

I also want to thank the entire team of the Wegener Center for Climate and Global Change for their warm welcome and the support they offered. The Wegener Center is really a very special place to work at.

Beyond that I am highly grateful to Michael Pock for creating the ready-made \LaTeX template I am using as I write these lines.

Last but not least I like to thank my whole family for supporting me during my years of study. Especially my parents, Helga and Gerald, who always encouraged me and never doubted my abilities. I am very grateful for all the freedom I had and of course the financial support they offered without hesitation.

Acronyms

Symbols

$\Delta\Delta T$ Delta-differential Transmission. 2, 3, 11, 19, 20, 37, 42, 43, 58, 61

A

ACCURATE Climate Benchmark Profiling of Greenhouse Gases and Thermodynamic Variables and Wind from Space—LMIO satellite mission. ix, 1, 13, 15, 24, 68

ACTLIMB Active Limb Sounding of Planetary Atmospheres [project]. 23

AEXPWIND Trace Gas Retrieval and Performance of Wind and Greenhouse Gas Profiling in the IRDAS-EXP/ACCURATE Context [ESA-ESTEC study, led by WEGC, UniGraz]. 1

aLoss Absorption Loss. 37

ATOMMS Active Temperature Ozone and Moisture Microwave Spectrometer. 1

D

dLoss Defocusing Loss. 37

E

ECMWF European Centre for Medium-Range Weather Forecasts. xiii, 24, 27–31, 67

EE8 Earth Explorer 8. 1

EGOPS End-to-End Generic Occultation Performance Simulation and Processing System. xii, 13, 23, 27

ESA European Space Agency. ix, x, 1

ESTEC European Space Research and Technology Centre. ix

F

FASCODE Fast-Atmospheric-Signature-Code. xiii, 10, 24, 27, 29–31, 67

FOM Forward Modelling. 24, 37, 42, 43, 48, 58, 61

G

GHG Greenhouse Gas. iii, 1–3, 6, 8, 10, 13–15, 17, 19, 20, 23–25, 27, 37, 67, 68

GNSS Global Navigation Satellite System. x, 1, 5

GPS Global Positioning System. 5

GRO Global Navigation Satellite System (GNSS) Radio Occultation. 1, 5, 6, 23

H

HITRAN High-Resolution Transmission [molecular spectroscopic database]. xiii, 8, 10, 13, 27, 28, 71

I

ILO Infrared-laser Occultation. x

IR Infrared. 5–7, 10, 13, 19, 23, 24, 27, 37, 42, 67, 68

IRDAS-EXP SWIR Long Range Differential Absorption Experiment for Trace Gas Measurements [ESA study, led by UoY]. ix, 1

L

l.o.s. line-of-sight. iii, v, 2, 3, 5–8, 10, 11, 13, 15–17, 19, 20, 28, 30, 31, 37, 38, 48, 53, 58, 61, 64, 69, 70

LEO Low Earth Orbit. iii, v, x, 1, 5–7, 16

LIO LEO–LEO Infrared-laser Occultation. 1–3, 5–7, 10, 11, 13, 15, 16, 19, 23–25, 27, 67

LMIO LEO–LEO Microwave and Infrared-laser Occultation. iii, 1, 3, 5–7, 13, 15, 29, 68, 69

LMO LEO–LEO Microwave Occultation. 1, 2, 5–7, 10, 13, 24, 25

M

x

MAP Mission Analysis/Planning. 24

MSR Multi-Line Trace Species Retrieval. 14, 15, 20

MW Microwave. 5–7, 13, 23, 24, 42

MWO Microwave Occultation. x

O

OPS Occultation Processing System. 24, 42, 43, 48, 58, 61

OSM Observation System Modelling. 23, 24, 37, 38, 42, 43, 48, 58, 69, 71

P

POD Precise Orbit Determination. 24

R

RFM Reference Forward Model. xiii, 10, 13, 19, 20, 27

RMS Root Mean Square. 15, 38

RO Radio Occultation. x, 1, 5

RX Receiver. 6–8, 10, 15–17, 31

S

SAW South Arctic Winter [atmosphere]. 2, 24, 28–30, 37, 38, 42, 43, 48, 58, 61, 67

SNR Signal-to-Noise Ratio. 38, 48, 58, 61, 64

SSR Single-Line Trace Species Retrieval. 13, 14, 19, 20

STD Standard [atmosphere]. 2, 24, 28–30, 37, 38, 42, 43, 48, 58, 61, 67

T

TP Tangent Point. 13

TRO Tropics [atmosphere]. 2, 24, 28–31, 37, 38, 42, 43, 48, 58, 61, 67

TX Transmitter. 6–8, 10, 15–17, 31

U

UniGraz University of Graz. ix, xi, 1

UoY University of York. x

UTLS Upper Troposphere–Lower Stratosphere [region]. iii, 15

V

VMR Volume Mixing Ratio. 13, 15

W

WEGC Wegener Center for Climate and Global Change [University of Graz]. ix, 1, 23

X

xEGOPS Experimental End-to-End Generic Occultation Performance Simulation and Processing System. 3, 13, 23, 24, 27, 30, 31, 67

Contents

Abstract	iii
Zusammenfassung	v
Acknowledgments	vii
Acronyms	ix
Introduction	1
1 LEO-LEO Microwave and Infrared-laser Occultation Method and Wind Observation Capability	5
1.1 LEO-LEO Microwave and Infrared-laser Occultation (LMIO) Method	5
1.2 Wind Retrieval Approach	7
1.2.1 General Approach	8
1.2.2 Simple Wind Retrieval	10
2 New Wind Profiling Algorithm	13
2.1 Basic Greenhouse Gas Retrieval Algorithm	13
2.2 New Wind Retrieval Algorithm	15
2.2.1 Mathematical Description	15
2.2.2 Implementation of the Algorithm	19
3 Setup of the Wind Simulations	23
3.1 General Setup	23
3.2 Data Setup	24
3.2.1 Fast-Atmospheric-Signature-Code (FASCODE) Atmospheres	25
3.2.2 Reference Forward Model (RFM) and High-Resolution Transmission (HITRAN) Database	27
3.2.3 European Centre for Medium-Range Weather Forecasts (ECMWF) Analysis Field	28
3.3 Atmospheric Conditions	28
3.4 Setup of Wind Cases	30

4 Wind Retrieval Results	37
4.1 General Performance of the new Abel Wind Retrieval	37
4.2 New Wind Retrieval in Synthetic Wind Conditions	42
4.2.1 Delta-differential Transmission in Synthetic Wind Conditions	42
4.2.2 L.o.s. Wind Velocity in Synthetic Wind Conditions	48
4.2.3 L.o.s. Wind Velocity Error in Synthetic Wind Conditions . .	53
4.3 New Wind Retrieval in Realistic Wind Conditions	58
4.3.1 Delta-differential Transmission in Realistic Wind Conditions	58
4.3.2 L.o.s. Wind Velocity in Realistic Wind Conditions	61
4.3.3 L.o.s. Wind Velocity Error in Realistic Wind Conditions . . .	64
Summary and Conclusion	67
List of Figures	69
List of Tables	71
Bibliography	73

Introduction

During the last decades the determination of geophysical variables in the Earth's atmosphere has been increasingly influenced by satellite measurements. Prior to the first satellite missions the atmospheric state only could be derived at relatively coarse spatial and temporal resolution (e.g., by radiosondes). This gave way to problems like bad coverage over the oceans or the southern hemisphere.

Now satellite measurements in general give us the opportunity to get global coverage while being less dependent on the ground properties at a high temporal resolution. Many advances have been made to retrieve the thermodynamic state variables of the atmosphere using the Global Navigation Satellite System (GNSS) Radio Occultation (GRO) method (e.g., Ware et al. (1996)) during the last years, and so GRO data contributes significantly to operational weather forecast models (e.g., Healy (2013)) and climate science (e.g., Steiner et al. (2011)).

A next step in the development of the occultation technique was the introduction of a microwave-based occultation method to retrieve the thermodynamic state variables in a similar fashion as in the GRO, but obtaining temperature and humidity separately, by Kursinski et al. (2002); Herman et al. (2004); Kursinski et al. (2009) (Active Temperature Ozone and Moisture Microwave Spectrometer (ATOMMS)) and by Kirchengast and Hoeg (2004); Gorbunov and Kirchengast (2005); Gorbunov and Kirchengast (2007); Schweitzer et al. (2011b) (LEO–LEO Microwave Occultation (LMO), between Low Earth Orbit (LEO) satellites).

Subsequently Kirchengast and Schweitzer (2011) proposed a method called LEO–LEO Microwave and Infrared-laser Occultation (LMIO). The LMO method was therein extended by a LEO–LEO Infrared-laser Occultation (LIO) part. LIO adds the capability of retrieving Greenhouse Gases (GHGs) and wind from space exploiting carefully selected absorption lines in the infrared spectrum. A proper algorithm for retrieving the GHGs was published by Proschek et al. (2011b).

The capability of the wind retrieval on the other hand was not the main focus of recent research. But Kirchengast and Schweitzer (2007) and Schweitzer (2010) already discusses a so-called *simple wind retrieval algorithm*.

The main goal of the present thesis is the discussion of a *new, more advanced wind retrieval algorithm*. The work for this thesis was done as part of the Trace Gas Retrieval and Performance of Wind and Greenhouse Gas Profiling in the IRDAS-EXP/ACCURATE Context (AEXPWIND) project at the Wegener Center for Climate and Global Change (WEGC), University of Graz (UniGraz).

The LMIO method was developed within the Climate Benchmark Profiling of Greenhouse Gases and Thermodynamic Variables and Wind from Space—LMIO satellite mission (ACCURATE) proposal supported by European Space Agency (ESA), which is a candidate for a new long-term global climate monitoring system for the Earth’s free atmosphere. The mission concept of ACCURATE is introduced in detail by Kirchengast and Schweitzer (2011); Schweitzer (2010) and was submitted as a proposal for the Earth Explorer 8 (EE8) mission by European Space Agency (ESA) (Kirchengast et al. 2010), where it received very good evaluation and was suggested for further studies.

The new wind algorithm is designated to derive the line-of-sight (l.o.s.) wind speed profile from LIO data. The GHG retrieval based on LMO and LIO for clear air (Proschek et al. 2011b) is used as a basis for the new wind retrieval.

The mentioned simple wind retrieval (Schweitzer 2010) is used as a comparison in this thesis. It uses the assumption of a constant wind velocity along the entire occultation ray path. The new wind retrieval on the other hand assumes a spherically symmetric distribution of the wind velocities around the tangent point location of the occultation event. Due to this assumption of local spherical symmetry, which is also much more realistic, the l.o.s. wind speed can be retrieved applying an Abel transform which was derived by Syndergaard and Kirchengast (2013).

Two wind frequency channels are defined at the absorption flanks of the *quasi-supersymmetric* $C^{18}OO$ absorption line. The two wind channels are located nominally $\pm 0.004 \text{ cm}^{-1}$ from the line center. Furthermore, a reference channel for both wind channels is defined, it is located off the absorption line, but spectrally close ($|(\lambda_{Wind} - \lambda_{Ref})/\lambda_{Ref}| < 0.1\%$) (Kirchengast and Schweitzer 2007).

Next the differential transmission (absorption signal minus reference signal) for each wind channels is calculated by subtracting the transmission at the reference channel from the transmission at the wind channels. Since both, absorption and reference channel, are influenced by atmospheric *broadband effects*, like defocusing and scintillation, the resulting differential transmissions is cleared from these effects with high fidelity (Schweitzer 2010; Schweitzer et al. 2011a).

Then the so-called *delta-differential transmission* ($\Delta\Delta T$) principle is applied, which means that two differential transmissions are subtracted from each other. The derived $\Delta\Delta T$ value is proportional to the wind-induced Doppler shift and it is used as the integrand value for the following Abel transform.

The performance of the new wind retrieval is investigated using synthetic and realistic l.o.s. wind profiles. In addition one set of polar satellite orbits (inclination = 90°) and one set of near-polar satellite orbits (inclination $\approx 80^\circ$) is tested.

This gives a total of ten wind setups, which are analyzed at three geographical locations. The first location is representing a dry and cold sub(ant)arctic atmosphere - South Arctic Winter (SAW). Furthermore there is an intermediate standard atmosphere - Standard (STD), and finally a moist and warm tropical atmosphere -

Tropics (TRO).

Besides the need for precise l.o.s. wind speed profiles themselves, the wind information will be used within the LIO retrieval to perform a correction of the GHG sensitive LIO center frequencies due to the wind-induced Doppler shifted frequencies. The infrared signal will be corrected for the wind-induced Doppler shift, therefore yielding more accurate GHG profiles in windy air.

The structure of the thesis is as follows. It starts in Chapter 1 with a presentation of the LMIO method (Kirchengast et al. 2010; Kirchengast and Schweitzer 2011; Schweitzer et al. 2011a; Proschek et al. 2011b) and the wind retrieval approach, including a discussion of the formerly used simple wind retrieval algorithm (Schweitzer 2010).

Chapter 2 follows with a description of the basic GHG retrieval algorithm (Proschek et al. 2011b) and the embedding of the new wind retrieval algorithm into the LIO algorithm as an added task. The part on the new wind algorithm covers the necessary mathematical calculation steps to derive the l.o.s. wind and then the frequency shift based on the $\Delta\Delta T$ from $C^{18}OO$ flank absorption lines (Syndergaard and Kirchengast 2013) and the implementation into the xEGOPS software as a stand alone module for the l.o.s. wind calculation (Plach et al. 2013).

Subsequently the setup for the wind simulations is described in Chapter 3, discussing the main input data sets and the investigated atmospheric conditions and wind profiles.

The simulation results are summarized in Chapter 4, giving a general performance review of the algorithm, and a discussion of the wind retrieval in synthetic and realistic wind conditions.

The thesis is closed by a summary and conclusion section.

1 LEO-LEO Microwave and Infrared-laser Occultation Method and Wind Observation Capability

The LEO-LEO Microwave and Infrared-laser Occultation (LMIO) method is a synergistic combination of the LEO-LEO Microwave Occultation (LMO) and the LEO-LEO Infrared-laser Occultation (LIO) techniques. The method was introduced in detail by Kirchengast et al. (2010), Schweitzer (2010) and Kirchengast and Schweitzer (2011). A detailed description of the algorithm for the LIO part was given by Proschek et al. (2011b), with the relevant atmospheric influences described by Schweitzer et al. (2011a). The LMIO is a proposed inter-satellite active limb-sounding technique which would be used to simultaneously retrieve the thermodynamic state variables, including pressure, temperature and humidity from LMO phase and amplitude data and a set of most important trace gas concentrations and the line-of-sight (l.o.s.) wind velocity from LIO intensity data. The method is discussed in more detail in Section 1.1. This is followed by a description of the wind retrieval approach in Section 1.2.

1.1 LEO-LEO Microwave and Infrared-laser Occultation (LMIO) Method

The LMO method alone can be seen as a next step in the development of the Global Navigation Satellite System (GNSS) Radio Occultation (GRO) method (Kursinski et al. 1997). GRO uses the two signals emitted by the Global Positioning System (GPS) and similar navigational satellites (decimeter-waves) to vertically scan the atmosphere, exploiting the occultation principle (Phinney and Anderson 1968; Kirchengast 2004). The receiving instruments are mounted on LEO satellites. GRO was successfully used to retrieve benchmark-quality refractivity profiles of the atmosphere in Ho et al. (2009) and atmospheric parameters like the temperature down to approximately 8 km of altitude, e.g., in Steiner et al. (2009), and more broadly in Steiner et al. (2013).

While the GRO method only uses the excess phase of the radio signal as a source of information, LMO in addition uses absorption of the MW amplitude and IR intensities applying the differential transmission principle (difference of an absorption

signal and a reference signal). The top of atmosphere vacuum signal and the fact of using H₂O absorption signals in the MW band makes the system self-calibrating and independent of background atmospheres to derive the specific humidity and the physical temperature (not only dry-temperature) (Schweitzer et al. 2011b).

In contrast to GRO where atmospheric background profiles are needed to retrieve a complete set of atmospheric state variables (pressure, temperature, humidity), LMO uses Transmitter (TX) and Receiver (RX) which are both mounted on LEO satellites. The LMO method was already developed to a sophisticated level (Kursinski et al. 2002; Kursinski et al. 2009; Herman et al. 2004; Kirchengast and Hoeg 2004; Schweitzer et al. 2011b). The LMIO method uses 5 frequency channels near the 22 and 183 GHz water vapor absorption lines for the LMO part (Kirchengast and Schweitzer 2011).

The novelty of the LMIO is the simultaneous measurement with IR-laser signals from the same platform as the MW signals. The proposed wavelength range is between 2 and 2.5 μm . In this range most of the major GHGs have absorption lines. A thorough search of target species absorption center frequency lines was done, and according reference lines which show the property of weak foreign target species absorption (Kirchengast and Schweitzer 2011; Schweitzer et al. 2011a). The IR differential transmission principle can therefore be used to derive profiles of certain GHGs and the l.o.s. wind velocity between TX and RX. The retrievable GHGs include H₂O (isotopes: HDO, H₂¹⁸O), CO₂ (isotopes: ¹³CO₂, C¹⁸OO), CH₄, N₂O, O₃, CO. As a compliment LIO can also be used to derive cloud layering (Proschek et al. 2011a), aerosol extinction, and turbulence strength (Kirchengast and Schweitzer 2011).

The geolocation information needed for the profiles is derived from LMO. Similar to GRO, precise satellite orbits and atmospheric excess phase data are used to get accurate altitude levels for every occultation ray path (ESA 2004). The corresponding uncertainty in altitude is between <10 to 20 m, likewise the horizontally location of the tangent point is known to a uncertainty of <1 km (Kursinski et al. 1997; Schweitzer et al. 2011b).

It is possible to use the LMO altitude information also for the LIO signal since the IR refractivity (Bönsch and Potulski 1998) in the used frequency range is almost non-dispersive and nearly identical to the MW refractivity (Thayer 1974). Due to these facts the LMO and the LIO signal propagation paths are almost congruent. This is true except for the lower atmosphere layers starting at 8 to 12 km where the humidity is increasing downwards. The H₂O leads to orientation polarization in the MW refractivity. The resulting difference can be accounted for by using the LMO-derived altitude and the thermodynamic profiles to construct the IR refractivity, the refraction angles, and the related LIO altitude levels (Proschek et al. 2011b).

The general LMIO geometry is shown in Figure 1.2. Two counter-rotating (indicated by black arrows) LEO satellites are orbiting the earth, this allows the atmo-

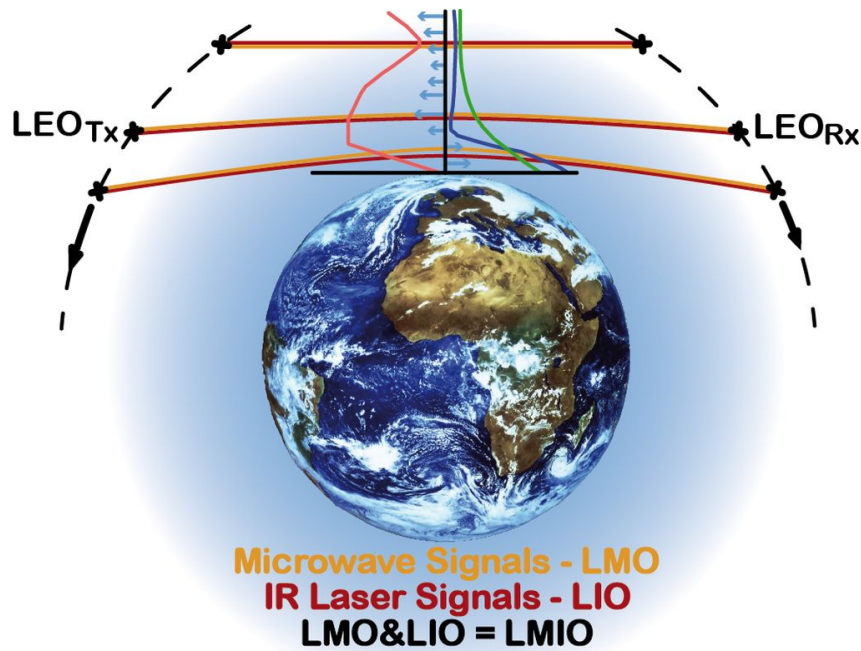


Figure 1.1: Schematic overview of LMIO geometry. Counter-rotating LEO satellites carrying Transmitter (TX) and Receiver (RX), respectively. The LMO occultation path is indicated in orange, while the LIO occultation path is red. The slightly different tangent point height in the lower atmosphere layers between IR and MW signal is also visible (from Schweitzer et al. (2011a))

sphere to be scanned vertically, facilitating the occultation principle (Phinney and Anderson 1968; Kirchengast 2004). The TX is sending IR and MW signals to the RX. The orange line indicates the MW and the red line the IR occultation path scanning through the atmosphere.

1.2 Wind Retrieval Approach

Here the general approach and the first method (in this thesis referred to as *simple wind retrieval*) to derive line-of-sight (l.o.s.) wind velocity from LIO is described. The l.o.s. wind direction is defined to be positive if the prevailing wind direction is from the Transmitter (TX) to the Receiver (RX). This section is similar to the subsection *Wind Retrieval* in Section 3.1.1 of Schweitzer (2010).

1.2.1 General Approach

If wind appears in the free atmosphere during a LIO event, the received IR signal is influenced. The wind induces a movement of the absorbing molecules towards or away from the TX, known as the Doppler effect. Thus a signal transmitted at a defined frequency appears relatively shifted for the moving absorbing molecules. The slightly shifted frequency is proportional to the prevailing l.o.s. wind speed. Furthermore the molecular absorption is observed at this shifted frequency. Most locations on Earth show meridional wind velocities within ± 30 m/s, this value corresponds to a relative frequency shift $\frac{\Delta f}{f}$ of the magnitude of 10^{-7} . The proposed LMIO method will mostly measure meridional wind speeds due to the occultation geometry caused by the near-polar satellite orbits used.

The frequency shift is exploited to retrieve the wind speed in the l.o.s. direction of the occultation path between the TX and the RX. Since the frequency shift is comparably small it is important to use parts of the absorption spectrum for the wind retrieval that are sensitive to small frequency changes as well. Hence inflexion points of an arbitrary symmetric absorption line can be used for the wind measurements. In more detail the l.o.s. wind velocity retrieval is based on the evaluation of the difference of two so-called wind channels (w_1 and w_2), which are located symmetrically displaced on the left and right hand side of the center of an absorption line. Wind channel w_1 is positioned at the inflexion point at the lower frequency side and wind channel w_2 at the higher frequency side of the absorption line.

The transmission spectrum of the $C^{18}OO$ absorption line used in this thesis is illustrated in Figure 1.2 in the left panel. In the right panel the corresponding first derivative is presented. Both variables, the transmission and the corresponding derivative, are shown for various tangent point heights between 5 and 35 km indicated by different colors. The position of the absorption line center and the two wind channels located at the inflexion points of the absorption line are marked with vertical lines. The $C^{18}OO$ absorption line was chosen because of its symmetric shape, its little dependence on pressure, temperature, and foreign GHG, and the fact that it is well-mixed globally and shows only small changes in concentration within the free atmosphere. The first derivative of the absorption line can be seen as an indicator of the sensitivity for frequency shifts.

To remove atmospheric broadband effects (e.g. scintillation caused by small-scale turbulence) the subtraction of the wind on-channels from its off-channel is performed. The reference signal is transmitted twice, once practically simultaneously with each wind channel.

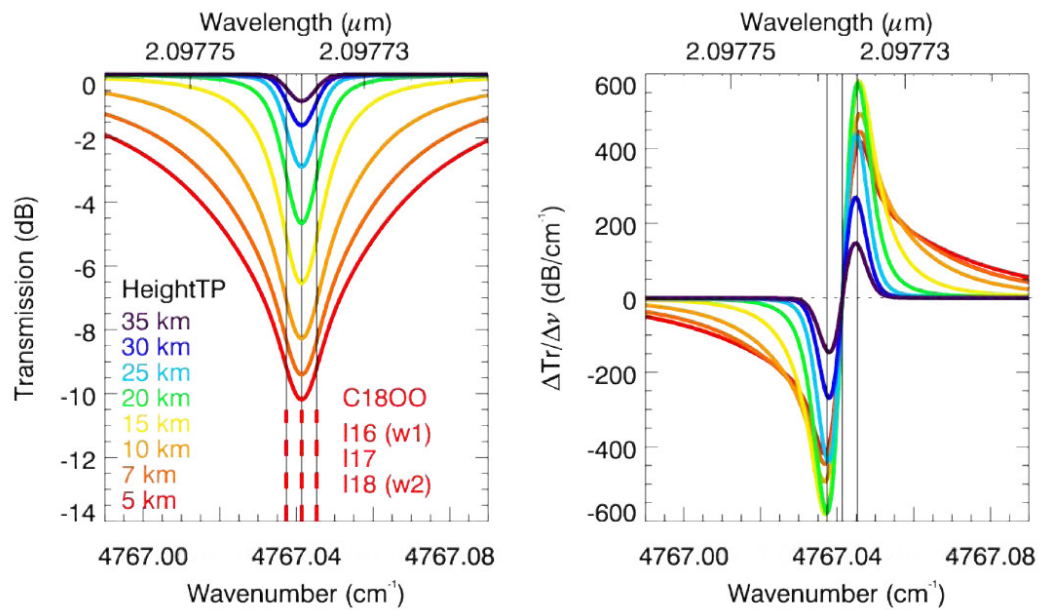


Figure 1.2: Left: Transmission spectrum of the $C^{18}OO$ absorption line which is used for the line-of-sight (l.o.s.) wind velocity retrieval (exemplary for HITRAN 2004). Right: The corresponding first derivative as a indicator for sensitivity to frequency shifts. Various tangent point heights are indicated by different colors. The position of the absorption line center and the two wind channels at the inflexion points are marked by vertical lines. (From Schweitzer (2010), Figure 3.4 therein)

1.2.2 Simple Wind Retrieval

The relation of l.o.s. wind velocity and frequency shift is as follows:

$$\overline{\Delta f} = -\frac{\overline{f}}{c_0} V_{l.o.s.} = -\frac{f_0}{c_0} V_{l.o.s.}, \quad (1.1)$$

where $\overline{\Delta f}$ is the mean wind-induced Doppler shift at the two wind channels $w1$ and $w2$. \overline{f} is the mean frequency of the two undisturbed wind channels. Since $w1$ and $w2$ are located symmetrically around the line center \overline{f} equals the center frequency of the absorption line f_0 . c_0 is the speed of light in vacuum and $V_{l.o.s.}$ is the l.o.s. wind speed. The negative sign is a result of the l.o.s. direction, which is defined from the TX to the RX. This means that if the absorbing molecules are moved away from the TX (positive wind speed) a negative frequency shift is induced, and the other way around. Since f_0 and c_0 are known, the $V_{l.o.s.}(z_{IR})$ profile can be derived from a $\overline{\Delta f}(z_{IR})$ profile, both being a function of the IR tangent point height z_{IR} . $\overline{\Delta f}(z_{IR})$ can be calculated from the transmission measurements (in dB) at the two wind channels ($T_{w1}(z_{IR})$ and $T_{w2}(z_{IR})$).

$$T_{wi} = T_{wi,0} + \left(\frac{dT}{df} \right)_{wi} \overline{\Delta f} \quad \text{with} \quad i = 1, 2 \quad (1.2)$$

$$\Delta T_{w1w2} = T_{w1} - T_{w2} \quad (1.3)$$

$$\Delta T_{w1w2,0} = T_{w1,0} - T_{w2,0} \quad (1.4)$$

$$\Delta T_{w1w2} = \Delta T_{w1w2,0} + \left(\left(\frac{dT}{df} \right)_{w1} - \left(\frac{dT}{df} \right)_{w2} \right) \overline{\Delta f} \quad (1.5)$$

$$\overline{\Delta f} = \frac{\Delta T_{w1w2} - \Delta T_{w1w2,0}}{\left(\frac{dT}{df} \right)_{w1} - \left(\frac{dT}{df} \right)_{w2}} \quad (1.6)$$

Equation (1.6) shows the result how to calculate $\overline{\Delta f}(z_{IR})$ from the observed Transmissions with the necessary intermediate steps in Equations (1.2) to (1.5). $T_{wi,0}$ is the transmission at the wind channels and $\left(\frac{dT}{df} \right)_{wi}$ the first spectral derivative of the transmission, both in calm air ($i = 1, 2$).

ΔT_{w1w2} is obtained from the measured transmissions T_{w1} and T_{w2} which are retrieved using LIO intensity data equivalent to the trace gas retrieval (Proschek et al. 2011b). The needed value $\Delta T_{w1w2,0}$ symbolizing calm air conditions is simulated. Therefore the Reference Forward Model (RFM) in combination with the High-Resolution Transmission (HITRAN) database, pressure and temperature profiles from the

LMO retrieval and GHG concentrations taken from the Fast-Atmospheric-Signature-Code (FASCODE) atmosphere or previous retrieval runs, are used to simulate $T_{w1,0}$, $T_{w2,0}$ and the corresponding derivatives $\left(\frac{dT}{df}\right)_{w1}$, $\left(\frac{dT}{df}\right)_{w2}$.

$\Delta T_{w1w2,0}$ should be zero if a perfectly symmetric absorption line is used. In practice this is never fully the case, since there are always influences by neighboring absorption lines to a certain extent. So $\Delta T_{w1w2,0}$ slightly differs from zero. Since Equation (1.2) to (1.6) still contain residual background effects, a final step is necessary. Forming the difference between the absorbing channels at the two wind frequencies and a reference channel, removes these background effects to a satisfactory degree. The so-called delta-differential transmission $\Delta\Delta T$ is calculated according to Equation (1.7).

$$\Delta\Delta T = (T_{w1} - T_{Ref}) - (T_{w2} - T_{Ref}) \quad (1.7)$$

Equation (1.8) finally is the major equation that is used in the *simple wind retrieval* discussed as a comparison in this thesis. This simple wind retrieval includes the *approximation of a constant l.o.s. wind velocity along the whole LIO ray path*. That is equivalent to a constant Doppler shift along the occultation path. In reality of course the wind velocity is varying if one follows the ray path and so is the Doppler shift. In the following chapter a *new wind retrieval* algorithm is introduced employing a *Abel Transform* and therefore accounting for the varying wind velocity.

$$V_{l.o.s.} = -\frac{c_o}{f_0} \overline{\Delta f} = -\frac{c_o}{f_0} \frac{\Delta\Delta T_{w1w2} - \Delta T_{w1w2,0}}{\left(\frac{dT}{df}\right)_{w1} - \left(\frac{dT}{df}\right)_{w2}} \quad (1.8)$$

2 New Wind Profiling Algorithm

In this chapter the *new wind retrieval algorithm* employing an *Abel Transform* is discussed. The chapter starts with a summary of the basic GHG retrieval algorithm in Section 2.1. The GHG retrieval is forming the backbone of the new wind retrieval algorithm. The following Section 2.2 is separated into a discussion of the necessary mathematical derivations to calculate the l.o.s. wind Subsection 2.2.1) and the implementation as a stand alone module into the xEGOPS software (Subsection 2.2.2).

2.1 Basic Greenhouse Gas Retrieval Algorithm

This section is giving an overview of the basic GHG retrieval algorithm on which the new wind retrieval algorithm is based. Similar descriptions are given in Proschek et al. (2011a) and Plach et al. (2013), both in Section 2.1 therein.

The so-called clear-air GHG retrieval (no clouds) is discussed in detail by Proschek et al. (2011b). Figure 2.1 shows the flow chart of the core LMIO algorithm with the position of the newly embedded wind algorithm (details see Section 2.2) framed in blue.

The MW excess phase and amplitude loss is used to derive the thermodynamic variables of pressure (p), temperature (T), and specific humidity (q). Furthermore the MW impact parameter is retrieved. This LMO part of the retrieval is framed in orange in Figure 2.1. A full description of the LMO retrieval, as it is implemented in the xEGOPS/EGOPS system is given in Schweitzer et al. (2011b). All the LMO retrieved variables are used as an input for the the LIO retrieval (GHGs and wind). This is also indicated with arrows from the LMO to the LIO part (red frame) in Figure 2.1. The LIO retrieval itself is mainly driven by the LIO intensities, sensitive to the absorption of GHGs and their isotopes. The ACCURATE mission design includes the measurement of H_2O , $^{12}\text{CO}_2$, $^{13}\text{CO}_2$, CH_4 , N_2O , O_3 , CO , C^{18}OO , H_2^{18}O , and HDO . But theoretically every species that has an absorption line within the considered IR spectrum between 2 and 2.5 μm can be retrieved if the signal structure is strong enough.

The so-called Single-Line Trace Species Retrieval (SSR) algorithm includes a step preparing the geometric parameters which is resulting in the Tangent Point (TP) altitude of the IR signal. Due to the different extent of interaction with the water vapor for IR and MW the corresponding TP altitudes differ slightly. The MW signal is more sensitive to water vapor and therefore is refracted stronger than the

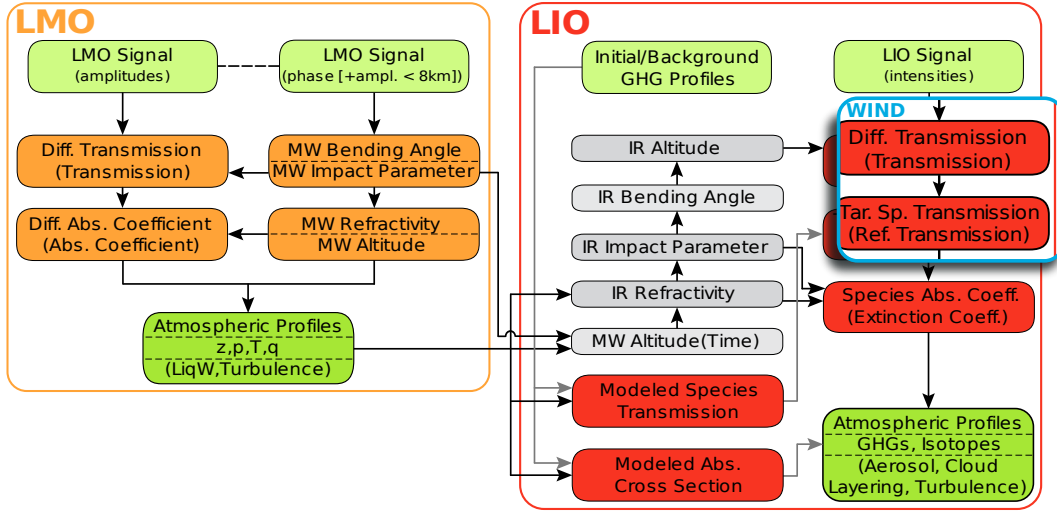


Figure 2.1: Schematic overview of the LMIO retrieval algorithm flow with the embedded new wind retrieval algorithm framed in blue. LMO part framed in orange. LIO part framed in red (modified from Proschek et al. (2011b), Figure 2 therein).

IR signal (Schweitzer et al. 2011a). The main step of the LIO algorithm is the calculation of the differential transmission. This is done by the differencing of an absorption and a reference IR signal pair (Figure 2.1 dyed red). Using this difference approach is resulting in a minimization of the unwanted broad-band effects on the IR signals (Rayleigh scattering, defocusing and spreading loss, aerosol extinction, and scintillation) (Schweitzer et al. 2011a). The absorption and reference signals can also be influenced by weak absorption of foreign GHG species. This fact is accounted for by subtracting a modeled foreign species transmission which is calculated using the Reference Forward Model (RFM) (Edwards 1996; Dudhia 2008) utilizing the High-Resolution Transmission (HITRAN) (Rothman et al. 2005; Rothman et al. 2009) line-by-line spectroscopic database. This so-called foreign species correction needs the atmospheric parameters from the LMO retrieval at the IR TP altitudes as well as an initial/background GHG. In a next step the resulting *pure* target species transmissions profile as a function of the TP altitude is converted to a corresponding absorption coefficient profile. Assuming spherical symmetry, this can be done with an Abel transform. In a last step the Volume Mixing Ratio (VMR) profiles of the investigated GHGs are derived from the absorption coefficient profiles (see Proschek et al. (2011b)).

To retrieve multiple GHG species the Multi-Line Trace Species Retrieval (MSR) is applied. It consists of several SSR steps using a predefined species retrieval order

(according to the consecutive foreign GHG influences). Every new retrieved profile is used to update the background GHG profiles for the foreign species correction to account for the co-dependence of next species on previously retrieved species.

In case of H₂O and CO₂ several profiles are combined using inverse-variance weighting. This is necessary to provide a sufficient sensitivity throughout the investigated Upper Troposphere–Lower Stratosphere (UTLS) region. The H₂O profile is composed of four H₂O(X) profiles and the CO₂ profile is joined from the two stable isotopes ¹²CO₂ and ¹³CO₂ (for more details see Proschek et al. (2011b)). After all these steps the retrieval yields GHG VMR profiles with a Root Mean Square (RMS) accuracies of within 1% to 3% and a vertical resolution of ≈1 km. To guarantee GHG profiles to converge to the best-estimate solution that is virtually independent of the initialization/background profiles, an outer loop over the full MSR scheme is introduced (basic-update-control loop).

2.2 New Wind Retrieval Algorithm

The “*quasi-supersymmetric*” C¹⁸OO absorption line, which is used for the new wind retrieval, is vulnerable to Doppler shift. As are all other GHG profiles which can be retrieved with the GHG retrieval algorithm discussed in Section 2.1 above.

Considering a frequency $f \approx 1.5 \times 10^{14}$ Hz ($\lambda \approx 2$ μm) the three major contributors to the Doppler shift show the following magnitudes: Doppler shift due to the motion of the TX and the RX ($\Delta f/f \approx 2.5 \times 10^{-5}$), the Earth’s rotation ($\Delta f/f \approx 1.5 \times 10^{-6}$), and the prevailing wind ($\Delta f/f \approx 1.0 \times 10^{-7}$) (Syndergaard and Kirchengast 2013). The Doppler shift caused by the motion of TX/RX and the Earth’s rotation can be predicted accurately, therefore they are supposed to be corrected automatically on-the-fly in a real satellite mission with a according transmitter frequency design. These corrections are considered in the LMIO mission proposal in Kirchengast et al. (2010).

The remaining Doppler shift mostly caused by the prevailing wind is adding a small error to the retrieved GHG profiles in case of windy air. But it can also be utilized to derive wind profiles of the LIO events, which, in a further step, can be used to correct this potential error of the GHG profiles.

Applying the new retrieval algorithm it is generally possible to derive l.o.s. wind velocities between ±1 m/s and ±100 m/s. This range covers all relevant wind speeds in the Earth’s atmosphere (Plach et al. 2013).

2.2.1 Mathematical Description

The formulation of the Abel Transform which is used for the new retrieval of the l.o.s. wind velocity from LIO data was done by Syndergaard and Kirchengast (2013). This subsection is similar to Chapter 2 therein.

General Remarks

Schweitzer (2010) introduced a so called *simple wind retrieval* within the ACCURATE mission concept. This simple wind retrieval uses the assumption of a constant wind velocity along the entire occultation ray path.

The *new wind retrieval* uses a more realistic assumption that the projection of the wind velocity vector into the occultation plane is following a great circle. This is equivalent to the wind blowing along spherical shells and a constant wind speed v at any altitude level z . In short that means it is assumed that the wind only shows a radial dependency $v(r)$ around the mean tangent point of a LIO event, with r being the distance from the center of the local spherical symmetry. Spherically symmetric problems like this can be solved utilizing an Abel transform.

Figure 2.2 is illustrating the wind blowing along spherical shells, with \vec{v} representing the projection of the wind velocity into the occultation plane. The figure also shows $\vec{v}_{||}$ which is the projection of \vec{v} onto the propagation direction. These two cases are discussed in Syndergaard and Kirchengast (2013) since they are slightly different. At the tangent point $v_{||} = v$. The figure is showing a positive l.o.s. wind velocity, since its direction is defined positive if the wind is blowing from the TX to the RX.

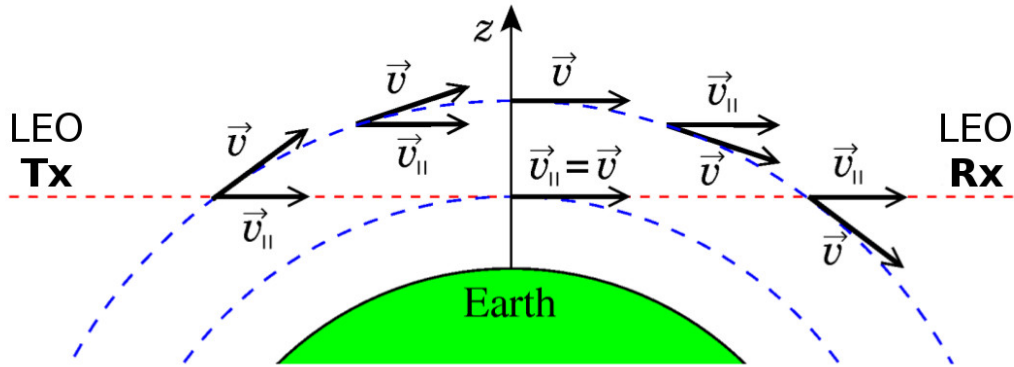


Figure 2.2: Illustration of a spherically symmetric wind velocity \vec{v} (here constant with altitude z , along spherical shells, blue-dashed), and its projection $\vec{v}_{||}$, along a ray path (red-dashed) between two LEO satellites. In reality the ray path is slightly bended which is not shown here. Exemplary shown for a positive l.o.s. wind velocity, being defined from TX to RX (modified from Syndergaard and Kirchengast (2013), Figure 2.1 therein).

Here we will only summarize the derivation of the Abel transform for \vec{v} since this is the more accurate assumption. Starting with the relation between relative Doppler shift $\frac{\Delta f}{f}$ and the causing velocity v

$$\frac{\Delta f}{f} \approx \frac{v}{c_0}, \quad (2.1)$$

where c_0 is the speed of light in vacuum, the wind-induced Doppler shift can be written as

$$\Delta f_{Wind} = -f_0 \frac{\vec{u} \cdot \vec{v}_{Wind}}{c_0} = -f_0 \frac{\vec{u} \cdot \vec{v}}{c_0} = -f_0 \frac{v_{||}}{c_0}, \quad (2.2)$$

where \vec{u} is the unit vector along the ray path at a certain point, v_{Wind} the wind velocity vector at this point, \vec{v} its projection into the occultation plane and $v_{||}$ the l.o.s. wind speed.

Equation for the new l.o.s. wind retrieval

The new wind retrieval starts with the transmissions at the two inflection points at the wings of the $C^{18}OO$ absorption line (nominally $\pm 0.004 \text{ cm}^{-1}$ from line center); the used frequencies are listed in Table 3.6 and Table 3.7 below. The transmissions are provided by the basic GHG retrieval algorithm discussed in Section 2.1 above.

The relation between the transmission T , the optical depth τ , and the volume absorption coefficient k is as follows:

$$\tau = \ln T = \int_{Tx}^{Rx} k ds. \quad (2.3)$$

To get the optical depth τ the volume absorption coefficient k is integrated over the whole ray path from TX to RX. k is a function of frequency, pressure, temperature, humidity, and GHG concentrations.

For the new wind retrieval this integration is done for the two frequencies at the inflection points around the $C^{18}OO$ absorption line (f_{w1} and f_{w2}) because the spectral derivative at these points is largest (Kirchengast and Schweitzer 2011).

The volume absorption coefficient $k(f_i)$ for a frequency f_i close to f_{wi} ($i = 1, 2$) can be written as

$$k(f_i) = k(f_{wi}) + \left. \frac{dk}{df} \right|_{f_{wi}} (f_i - f_{wi}). \quad (2.4)$$

Assuming f_1 and f_2 being Doppler shifted by wind we can further write

$$k(f_i) = k(f_{wi}) - f_{wi} \left. \frac{dk}{df} \right|_{f_{wi}} \frac{v_{||}}{c_0}, \quad (2.5)$$

again $i = 1, 2$ for the corresponding wind frequencies. As a next step it is necessary to calculate the difference between the absorption coefficients at the two inflection points Δk , with

$$\Delta k_0 = k(f_{w2}) - k(f_{w1}) \quad (2.6)$$

and

$$\Delta \chi_0 = f_{w2} \frac{dk}{df} \Big|_{f_{w2}} - f_{w1} \frac{dk}{df} \Big|_{f_{w1}}. \quad (2.7)$$

Δk can be written as

$$\Delta k = k(f_2) - k(f_1) = \Delta k_0 - \Delta \chi_0 \frac{v_{||}}{c_0}. \quad (2.8)$$

The optical depth difference following from Equation (2.8) looks like

$$\Delta \tau = \int_{Tx}^{Rx} \Delta k_0 ds - \frac{1}{c_0} \int_{Tx}^{Rx} \Delta \chi_0 v_{||} ds. \quad (2.9)$$

The two introduced differential parameters Δk_0 and $\Delta \chi_0$ represent the case of no wind and need to be known for example from an independent measurement of the $C^{18}O$ concentration. Due to the only small difference between the f_i and the f_{wi} , disturbing effects like scintillation and defocusing are removed to a high extent in $\Delta \tau$ from real measurements.

As discussed before we use the assumption that $v = v(r)$ (corresponding refractive index $n = n(r)$ and differential absorption coefficient $\Delta k_0 = \Delta k_0(r)$). Using Bouguer's law,

$$v_{||} = \frac{av(r)}{rn(r)}, \quad (2.10)$$

and

$$ds = \frac{rn(r)dr}{\sqrt{r^2n^2(r) - a^2}}, \quad (2.11)$$

where a is the impact parameter, and the substitution $x = rn(r)$, we can write $\Delta \tau$ as follows:

$$\Delta \tau(a) = 2 \int_a^\infty \frac{x \Delta k_0(x) \frac{dr}{dx} dx}{\sqrt{x^2 - a^2}} - 2 \frac{a}{c_0} \int_a^\infty \frac{\Delta \chi_0(x) v(x) \frac{dr}{dx} dx}{\sqrt{x^2 - a^2}}. \quad (2.12)$$

If the used absorption line is perfectly symmetric Δk_0 is zero. In reality this is never fully the case since there is always an influence by neighboring absorption lines to a certain extent (Schweitzer 2010). By defining

$$\delta(a) = 2 \int_a^\infty \frac{x \Delta k_0(x) \frac{dr}{dx} dx}{\sqrt{x^2 - a^2}}, \quad (2.13)$$

we can solve for v using an Abel transform:

$$v(a) = \frac{c_0}{\Delta\chi_0(a)} \frac{1}{\pi} \frac{d}{dr} \int_a^\infty \frac{(\Delta\tau(x) - \delta(x))dx}{\sqrt{x^2 - a^2}}. \quad (2.14)$$

But, we can also write

$$\delta(a) = 2 \int_a^\infty \frac{a\Delta k_0(x) \frac{dr}{dx} dx}{\sqrt{x^2 - a^2}} + \epsilon(a), \quad (2.15)$$

with

$$\epsilon(a) = 2 \int_a^\infty \frac{\sqrt{x-a}}{\sqrt{x+a}} \Delta k_0(x) \frac{dr}{dx} dx. \quad (2.16)$$

$\epsilon(a)$ can be ignored since it is very small. We finally arrive at the approximate relation between $v(a)$ and $\Delta\tau(x)$ if Δk_0 and $\Delta\chi_0$ are known:

$$v(a) \approx \frac{c_0}{\Delta\chi_0(a)} \left[\frac{1}{\pi} \frac{d}{dr} \int_a^\infty \frac{\Delta\tau(x)dx}{\sqrt{x^2 - a^2}} + \Delta k_0(a) \right]. \quad (2.17)$$

2.2.2 Implementation of the Algorithm

The implementation of the new wind retrieval algorithm was discussed in Plach et al. (2013). This section is similar to Section 2.2.2 therein.

Like mentioned above, the new wind algorithm starts with an intermediate product, the differential species transmission, provided by the SSR (see Section 2.1). To give an overview, Figure 2.3 shows the part of the LIO retrieval where the new wind retrieval is embedded (indicated in blue).

The algorithm starts with a smoothing of the target species transmissions for the two wind channels, which is provided at the IR altitude grid from the preparatory steps from the SSR (for details see Proschek et al. (2011b)). The target species transmission is calculated by subtracting the reference signal from an absorption signal and performing the GHG correction as suggested by Proschek et al. (2011b). The smoothing is done with a sliding polynomial filter (3rd order). The filter width is chosen to be approximately 1 km. As the next step the delta-differential transmission ($\Delta\Delta T$) is derived from the differential transmissions at the two wind channels (ΔT_{fw1} and ΔT_{fw2}):

$$\Delta\Delta T = \Delta T_{fw1} - \Delta T_{fw2}. \quad (2.18)$$

In the following paragraphs $i = 1$ is equivalent to wind channel 1 and $i = 2$ is corresponding to wind channel 2. The volume absorption coefficients $k(f_{wi\pm h})$ are derived using the external RFM. The RFM is called four times to get the corresponding absorption coefficients \pm an increment h displaced from each of the two

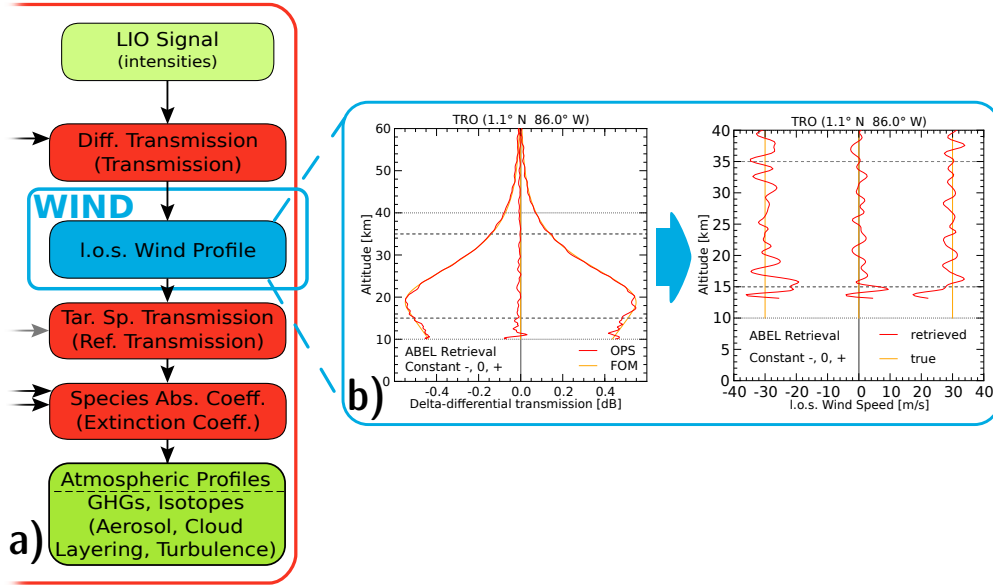


Figure 2.3: a) Section of the LIO retrieval algorithm with the wind retrieval step inserted (blue). b) Example of a delta-differential transmission ($\Delta\Delta T$) profile on the left and the subsequently retrieved l.o.s. wind profiles on the right (modified from Plach et al. (2013)).

wind channels. From these values the derivatives $\frac{dk}{df} \Big|_{f_{wi}} = \frac{k(f_{wi+h}) - k(f_{wi-h})}{2h}$ and subsequently the variable $\Delta\chi_0(a)$ (Equation (2.7)) are computed.

For the variable $\Delta k_0(a)$ the absorption coefficients at the wind channels $k(f_{wi})$ are needed. For computational efficiency they are computed by forming the arithmetical mean between the two enveloping coefficients ($k(f_{wi+h})$, $k(f_{wi-h})$) which are known from the preceding RFM calls. It can be shown that the derived values are virtually identical to an actual RFM call at the frequencies f_{wi} . The differences are negligible since the $C^{18}OO$ absorption line is symmetrical to a very high degree. As a last step before the core of the algorithm (the Abel transform) is performed, the $\Delta\Delta T$ is smoothed applying the same filter as noted above.

To finally get the l.o.s. wind velocity from the $\Delta\Delta T$, representing $\Delta\tau$, and the simulated absorption coefficients k the Abel integral in Equation (2.17) needs to be solved numerically. This is done with a similar routine as in Schweitzer et al. (2011b) but adopted to the integrand needs. After this calculation and a final smoothing (again with the polynomial filter) of the l.o.s. wind velocity, it is written to an output file. In further processing steps the l.o.s. wind profile can be used

correct frequencies of further target species calculations with the l.o.s. wind-induced Doppler shift to continue the SSR and thus the MSR for the GHGs.

3 Setup of the Wind Simulations

The analyzed wind simulations are those described in Plach et al. (2013). This chapter is similar to Chapter 3 therein.

All simulations for this thesis are done with the xEGOPS software applying quasi-realistic atmospheric conditions for the propagation of the MW and the IR signal.

This chapter is focusing on the setup, which is necessary for the performance analysis of the later discussed wind simulations. It starts with the general setup, including a short description of the software xEGOPS and the settings used (Section 3.1). This is followed by a discussion of the data basis in Section 3.2 and of the atmospheric conditions in Section 3.3. The chapter is concluded with the selected wind profiles used for the forward simulations in Section 3.4.

A simplified performance analysis of the new wind retrieval was done by Syndergaard and Kirchengast (2013). The main differences between the analysis in the present thesis and this simplified analysis are: real ray-tracing instead of a straight-line propagation ($\frac{dr}{dx} = 1$), realistic atmospheric conditions (see Section 3.2) instead of an isothermal atmosphere at 240 K, synthetic and realistic wind profiles contrary to only synthetic wind profiles, and finally the superimposition of realistic observation errors onto the forward-modeled signal (using the Observation System Modelling (OSM)) compared to no error model.

3.1 General Setup

For the simulations in this thesis a software called Experimental End-to-End Generic Occultation Performance Simulation and Processing System (xEGOPS) is used. It is a subsidiary of the End-to-End Generic Occultation Performance Simulation and Processing System (EGOPS), which is used to perform end-to-end simulations and retrievals of thermodynamic state variables (pressure, temperature, and humidity) from GRO data sets. Both programs were developed at the Wegener Center for Climate and Global Change (WEGC) in cooperation with international partners.

xEGOPS is a software package that enables the implementation of new algorithms in a test phase and uses the EGOPS as a kernel library. It therefore provides the environment for parallel development of both systems. xEGOPS adds the capability of simulating LIO events in an end-to-end fashion. xEGOPS was developed within the frame of the Active Limb Sounding of Planetary Atmospheres (ACTLIMB)

project. A detailed documentation of the EGOPS and the xEGOPS software can be found in Fritzer et al. (2009) and Fritzer et al. (2010), respectively. A description of the GHG retrieval, which is the backbone of the new wind retrieval algorithm is given in Section 2.1 above.

To simulate the geometric trajectories and therefore yielding the geographic distribution of the tangent point location for the occultation events the Mission Analysis/Planning (MAP), a sub-tool of xEGOPS, is used. This was done for two sets of satellite orbits, which are summarized in Table 3.1 and Table 3.2. The first orbits are chosen to give an exact one-to-one comparison between the new wind retrieval and the simple wind retrieval discussed in Schweitzer (2010) which utilizes the identical orbits (polar orbits with an inclination of 90°). The second set of orbits is taken from the final proposal of the ACCURATE mission concept (Kirchengast et al. 2010) and is representing a baseline for an actual future satellite mission. They are near-polar orbits with an inclination of $\approx 80^\circ$. The global distribution of the occultation events for the polar orbits is presented in Figure 3.1 and for the near-polar orbits in Figure 3.2.

For each set of satellite orbits three events are selected to represent different atmospheric conditions (see Section 3.3). These locations are given in Table 3.3.

The propagation of the LMO and the LIO signals was simulated with the Forward Modelling (FOM) sub-system of the xEGOPS. An elliptical Earth model (WGS-84 ellipsoid) and a sampling rate of 10 Hz is used for the simulations. MW and IR signals are, besides refraction, attenuated by molecular absorption and defocusing loss. The IR signals are additionally weakened by Rayleigh scattering and medium aerosol extinction (see Schweitzer et al. (2011a)).

In the next step realistic observational errors are superimposed on the forward-modeled signals (up to here only effects of atmospheric propagation) by the xEGOPS-Observation System Modelling (OSM). These errors include Precise Orbit Determination (POD) errors, thermal noise, intensity drift, and finitely precise clock errors; in the present thesis no clock errors are simulated. The applied error settings are summarized in Table 3.5 for the MW part and in Table 3.4 for the IR part.

The last step of the end-to-end simulations is the retrieval of the thermodynamic variables (temperature, pressure, and humidity) and altitude information from LMO data (see (Schweitzer et al. 2011b)), and the GHG (see (Proschek et al. 2011b)) and wind profiles from LIO data. This is done by the Occultation Processing System (OPS) subsystem of the xEGOPS.

3.2 Data Setup

This section is giving an overview of the input data for the model atmosphere used for the end-to-end simulations performed with xEGOPS.

Table 3.1: Settings for the RX and TX using polar orbits

	TX1	TX2	RX1	RX2
Satellite Height	800 km		650 km	
Orbit Inclination	90.0°		90.0°	
Right Ascension of the Ascending Node	0.0°		180.0°	
Eccentricity	0.0001		0.0001	
Argument of Perigee	90.00°		90.00°	
Mean Anomaly	0.00°	180.00°	0.00°	90.00°

Table 3.2: Settings for the RX and TX using near-polar ($i \approx 80^\circ$) orbits

	TX1	TX2	RX1	RX2
Satellite Height	595 km		512 km	
Orbit Inclination	80.0°		80.4°	
Right Ascension of the Ascending Node	0.0°		180.0°	
Eccentricity	0.0001		0.0001	
Argument of Perigee	90.00°		90.0°	
Mean Anomaly	0.00°	180.00°	40.00°	120.00°

3.2.1 Fast-Atmospheric-Signature-Code (FASCODE) Atmospheres

The Fast-Atmospheric-Signature-Code (FASCODE) is an atmospheric model utilizing US standard atmospheres (Anderson et al. 1986). According to the latitude of the mean tangent point of an occultation event one of the localized atmospheres provided is used: Tropics (TRO), Standard (STD), or South Arctic Winter (SAW). The FASCODE version used is the one provided online (FASCODE 2008). It supplies profiles of the thermodynamic variables pressure, temperature, and humidity. Furthermore profiles of O_2 and most major GHGs are provided including H_2O , HDO, $H_2^{18}O$, $^{12}CO_2$, $^{13}CO_2$, $C^{18}OO$, O_3 , N_2O , CO , CH_4 . The concentration of the secondary isotopes is calculated from the primary isotopes concentration using fractional abundances according to Rothman et al. (2005).

All profiles are supplied at altitude levels from 0 to 120 km. The increment is increasing from surface to atmosphere top. From 0 to 25 km it is 1 km, 25 to 50 km 2.5 km, and from 50 to 120 km 5 km. The included CO_2 concentration up to the mesopause was changed from 330 ppmv (appropriate for the early 1980's) to a more recent value of 380 ppmv (also see Kirchengast and Schweitzer (2011)).

The atmosphere is a so-called clear-air setting, which means it is free of clouds. From this fact it follows that refraction, defocusing, and GHG trace species absorption are the main processes contributing to the simulated LMO excess phase, LMO amplitude loss, and LIO intensity loss data. Rayleigh scattering and aerosol

3 Setup of the Wind Simulations

Table 3.3: Atmosphere and forward simulation settings

Atmosphere	Tropical (TRO)	Standard (STD)	Sub-Arctic Winter (SAW)
Atmosphere model	FASCODE / ECMWF analysis field		
Effects	clear air, including: molecular absorption, aerosol extinction, Rayleigh scattering, defocusing loss		
Atmospheric structure	Spherical symmetry @ event location		
Date of Event	July 15 th , 2007		
Polar orbits			
Occ. Event Numbers	100	118	040
Position	1.1 °N, 86.0 °W	39.7 °N, 114.0 °W	67.5 °S, 7.3 °E
Near-polar orbits			
Occ. Event Numbers	021	211	095
Position	8.4 °N, 158.7 °W	47.9 °N, 91.8 °W	66.6 °S, 81.7 °E
ECMWF File name	ecmwf-analyses-T511-20070715121.grb		
Forward Simulation Settings			
Propagation simulator	Full-3D Ray Tracer (sampling rate 10 Hz) ray tracer at highest available accuracy level		
Vertical simulation range	3 km to 80 km		
Earth shape	Ellipsoidal Earth (WGS84)		

Table 3.4: OSM Instrumental errors for LIO RX and TX

LIO Error Source	Details
Kinematic POD error	applying random drifts (as RMS) assuming radial position error of LEO-TX and LEO-RX satellites of 0.25 m, along ray velocity error of 0.05 mm s^{-1} and along ray acceleration error of $0.05 \mu\text{m s}^{-2}$
Thermal noise error	assuming reception loss of 1.25 dB, total optical loss of 1.87 dB, noise equivalent RX power of -124.9 dB W
Polynomial intensity drift error	linear drift of 0.04 dB min^{-1} , downwards from reference height (reference height: 35 km)
Clock errors	perfect clocks (no differencing)

Table 3.5: OSM Instrumental errors for LMO RX and TX

LMO Error Source	Details
Kinematic POD error	applying random drifts (as RMS) assuming radial position error of LEO-TX and LEO-RX satellites of 0.25 m, along ray velocity error of 0.05 mm s^{-1} and along ray acceleration error of $0.05 \text{ } \mu\text{m s}^{-2}$
Thermal noise	no CXK-Band thermal noise
Polynomial intensity drift error	no polynomial drifts
Clock errors	perfect clocks (no differencing)

extinction loss are also simulated (Prosczek et al. 2011b).

The FASCODE thermodynamic variable profiles are used for every discussed setup, except the realistic cases using the near-polar orbits. In these cases the thermodynamic variables were taken from the ECMWF analysis field.

The GHG concentration profiles for every discussed setup are taken from the FASCODE atmosphere with no exceptions since the ECMWF analysis field is not supplying any GHGs.

3.2.2 Reference Forward Model (RFM) and High-Resolution Transmission (HITRAN) Database

The molecular absorption in the considered IR range from 2 to $2.5 \text{ } \mu\text{m}$ needed for the absorption coefficients at the LIO channels are calculated using the Reference Forward Model (RFM) (Edwards 1996; Dudhia 2008), which is integrated in the xEGOPS/EGOPS. RFM is a line-by-line radiative transfer model developed at the Oxford University. The spectroscopic parameters for all considered absorption lines (absorption line center frequencies, line widths,...) are taken from the High-Resolution Transmission (HITRAN) database (Rothman et al. 2005).

Since the wind setup using the polar orbits is thought to provide a comparison with a former study in Schweitzer (2010), the same HITRAN version of 2004 (Rothman et al. 2005) is used. The wind setup with near-polar orbits represents a more recent proposal (Kirchengast et al. 2010) and therefore uses the HITRAN 2008 database (Rothman et al. 2009).

A small modification to the HITRAN 2008 database is done here. Starting with this version, a pressure shift parameter was introduced for the C^{18}O absorption line. Not all modules of the used xEGOPS system are yet able to deal with the resulting altitude dependency and it is not very worthwhile to implement, since the pressure shift will in reality be automatically corrected by transmitter frequency design. HITRAN 2008 is therefore used with the modification of a pressure shift parameter value which was intentionally set to zero for the C^{18}O absorption line.

Table 3.6: Absorption and reference channels - polar orbits (HITRAN 2004).

Channel ID	Channel utility	Wavenumber [cm ⁻¹]	Frequency [Hz]
I16	Abs[C ¹⁸ OO-w ₁], l.o.s. wind	4767.037412	1.429 121 863 241 36 × 10 ¹⁴
I17	Abs[C ¹⁸ OO]	4767.041369	1.429 123 049 400 20 × 10 ¹⁴
I18	Abs[C ¹⁸ OO-w ₂], l.o.s. wind	4767.045326	1.429 124 235 559 03 × 10 ¹⁴
I19	Ref[l.o.s. wind]	4770.150000	1.430 054 993 528 70 × 10 ¹⁴

Table 3.7: Absorption and reference channels - near-polar orbits (HITRAN 2008).

Channel ID	Channel utility	Wavenumber [cm ⁻¹]	Frequency [Hz]
I16	Abs[C ¹⁸ OO-w ₁], l.o.s. wind	4767.037455	1.429 121 876 012 51 × 10 ¹⁴
I17	Abs[C ¹⁸ OO]	4767.041455	1.429 123 075 182 35 × 10 ¹⁴
I18	Abs[C ¹⁸ OO-w ₂], l.o.s. wind	4767.045455	1.429 124 274 352 18 × 10 ¹⁴
I19	Ref[l.o.s. wind]	4770.150000	1.430 054 993 528 70 × 10 ¹⁴

All the frequency channels used for the present study are summarized in Table 3.6 and Table 3.7.

3.2.3 European Centre for Medium-Range Weather Forecasts (ECMWF) Analysis Field

To provide realistic profiles of wind velocity and thermodynamic variables an European Centre for Medium-Range Weather Forecasts (ECMWF) analysis field from July, 15th 2007 is used. It has a horizontal resolution of approximately 40 km (T511) and 91 vertical levels with increasing increments further up in the atmosphere. The file name is listed in Table 3.3; details on ECMWF data products can be found at <http://www.ecmwf.int>.

3.3 Atmospheric Conditions

This thesis investigates the l.o.s. wind profiles for three different atmospheric conditions representing three different geographical locations. This investigation is done for each of the two sets of satellite orbits discussed in Section 3.1, which gives a total of six analyzed occultation events.

The atmospheric conditions are: Tropics (TRO) - a warm and moist atmosphere in the tropics, Standard (STD) - an intermediate atmosphere at mid-latitudes, and South Arctic Winter (SAW) - a cold and dry atmosphere near the antarctic circle.

The events are chosen to tentatively show high-end wind speeds and variable vertical wind shear to demonstrate the capability of the new retrieval under challenging wind conditions.

For most cases the atmospheric state variable profiles are provided by the FASCODE atmosphere and are combined with synthetic wind profiles and realistic wind profiles from an ECMWF analysis field. Just the near-polar setup with realistic wind profiles uses atmospheric state variables also from the corresponding ECMWF analysis field (see Subsection 3.2.1).

To conclude this section, the global distribution of the occultation events on the investigated day (July 15th, 2007) are shown in Figure 3.1 for the polar satellite orbits. The three events which are used are indicated in the figure. The date, the orbits and the locations are intentionally the same as in in Schweitzer (2010), so a one-to-one comparison between the simple wind retrieval (also discussed in Schweitzer (2010)) and the new wind retrieval introduced here, and a back-verification, can be done.

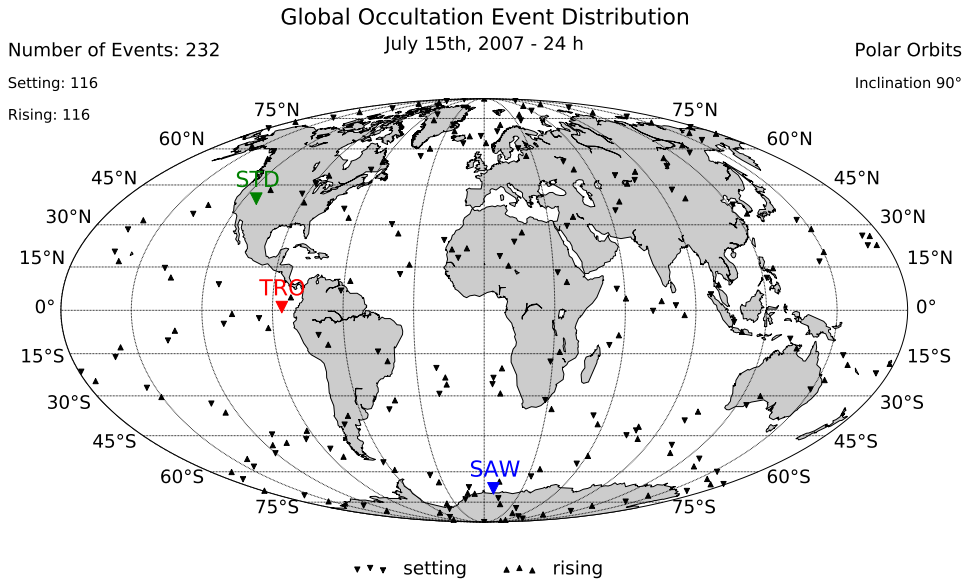


Figure 3.1: Global distribution of the occultation events on July 15th, 2007 using polar orbits. Rising events are indicated with upright triangles, while setting events are represented using reversed (upside-down) triangles. The three geographic locations respectively occultation events used for the analysis are colored: **TRO**, **STD**, **SAW**.

The same global distribution of the occultation events (also the same day), but for a more recent set of near-polar satellite orbits, with an inclination of $\approx 80^\circ$,

3 Setup of the Wind Simulations

is illustrated in Figure 3.2. This new set of near-polar orbits is the most recent choice for a future LMIO satellite mission (Kirchengast et al. 2010). The slightly lower satellite orbits (compare Table 3.1 and Table 3.2) yield slightly shorter orbital periods and as a result show some more occultation events each day.

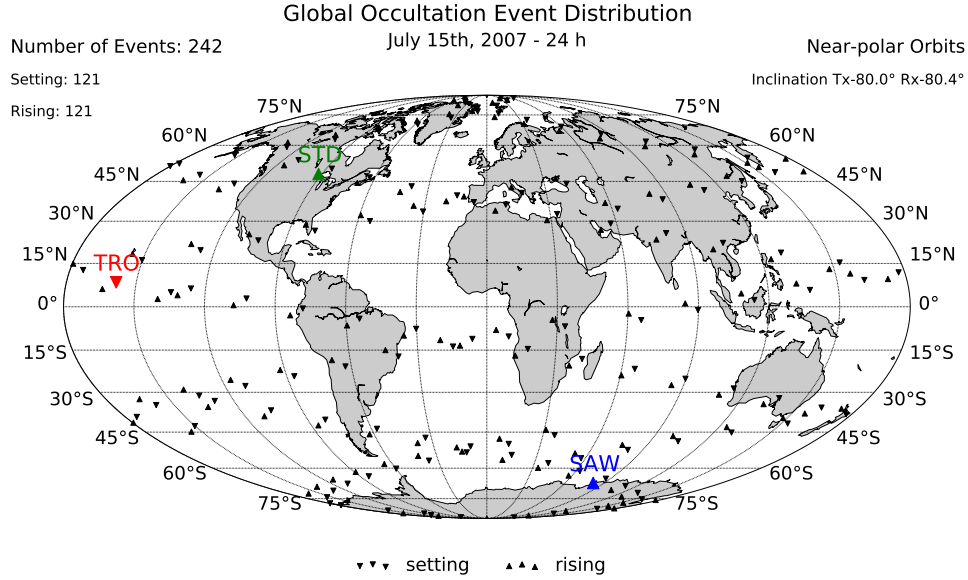


Figure 3.2: Global distribution of the occultation events on July 15th, 2007 using near-polar orbits. Rising events are indicated with upright triangles, while setting events are represented using reversed (upside-down) triangles. The three geographic locations respectively occultation events used for the analysis are colored: **TRO**, **STD**, **SAW**.

3.4 Setup of Wind Cases

Generally two types of wind profiles are analyzed in this thesis. First these are synthetic wind profiles - a constant positive (+30 m/s), a constant negative (-30 m/s), a sinusoidal alternating (± 30 m/s), and a no wind profile. The synthetic wind profiles only have a meridional and no zonal wind component. The synthetic profiles for both investigated satellite orbits (polar and near-polar) are illustrated on the right side in Figure 3.3 and Figure 3.4. The figures show the meridional and zonal wind components in light colors and the true l.o.s. wind profiles in dark colors. All three locations (see Section 3.3) are presented. The TRO atmosphere at the top,

STD in the middle, and SAW at the bottom. As an additional information the used FASCODE temperature profiles are plotted on the left side.

The second type of profiles are realistic wind profiles taken from an ECMWF analysis field (see Subsection 3.2.3), including both meridional and zonal wind components. The realistic wind profiles are presented in Figure 3.5 and Figure 3.6, again for both sets of satellite orbits and all locations. The figures follow the same color scheme as for the synthetic cases above. The corresponding temperature profiles on the left are from FASCODE in case of the polar orbits, and from the ECMWF analysis field in case of the near-polar orbits (see Section 3.3).

Looking at the figures in this section, it is evident that, in case of polar orbits, the l.o.s. is perfectly north/south oriented, and so the meridional wind component is identical to the l.o.s. wind velocity. There is no contribution from the (zero) zonal component. The mirrored looks of the l.o.s. and the meridional wind in most cases, except the near-polar TRO case, can be explained as follows. It is caused by the relative definition of the l.o.s. wind direction in dependence to the position of the TX and the RX to each other and the absolute definition of the wind directions provided by the ECMWF analysis field. As defined in Section 1.2 the l.o.s. wind direction is positive if the prevailing wind is blowing towards the RX. In the ECMWF field on the other hand a positive wind is blowing from south to north. From this different definitions it follows that in case the RX is south of the TX, the true wind and the retrieved l.o.s. wind show opposite signs. This happens for all three events using the polar satellite orbits (see Figure 3.3 and Figure 3.5).

The near-polar TRO case illustrated in Figure 3.4 and Figure 3.6 at the top show the opposite constellation. The TX is south of the RX resulting in the same sign of meridional and the l.o.s. wind.

Another interesting feature which can be seen in the figures in this section is the influence of the inclination of the used satellite orbits and the resulting tilt of the l.o.s. direction, i.e., the deviation of the l.o.s. direction from the meridional direction. Comparing the figures showing the synthetic wind cases for polar and near-polar orbits it is evident that the mentioned tilt is increasing with latitude. Since there are no zonal wind components for the synthetic wind profiles this can be seen especially nicely. In Figure 3.3 all retrieved l.o.s. wind profiles are identical with the meridional wind components (polar orbits). Looking at Figure 3.4 (near-polar orbits) the TRO case is still fairly meridional, not much difference between the retrieved l.o.s. wind and the true wind. With increasing latitude the l.o.s. is tilted in favor of the zonal wind component. This tilt is resulting in the retrieved l.o.s. wind being smaller than the input meridional wind, since the l.o.s. is not perfectly meridional anymore. The contribution of the zonal wind component can be seen in Figure 3.5 where it is non-zero.

3 Setup of the Wind Simulations

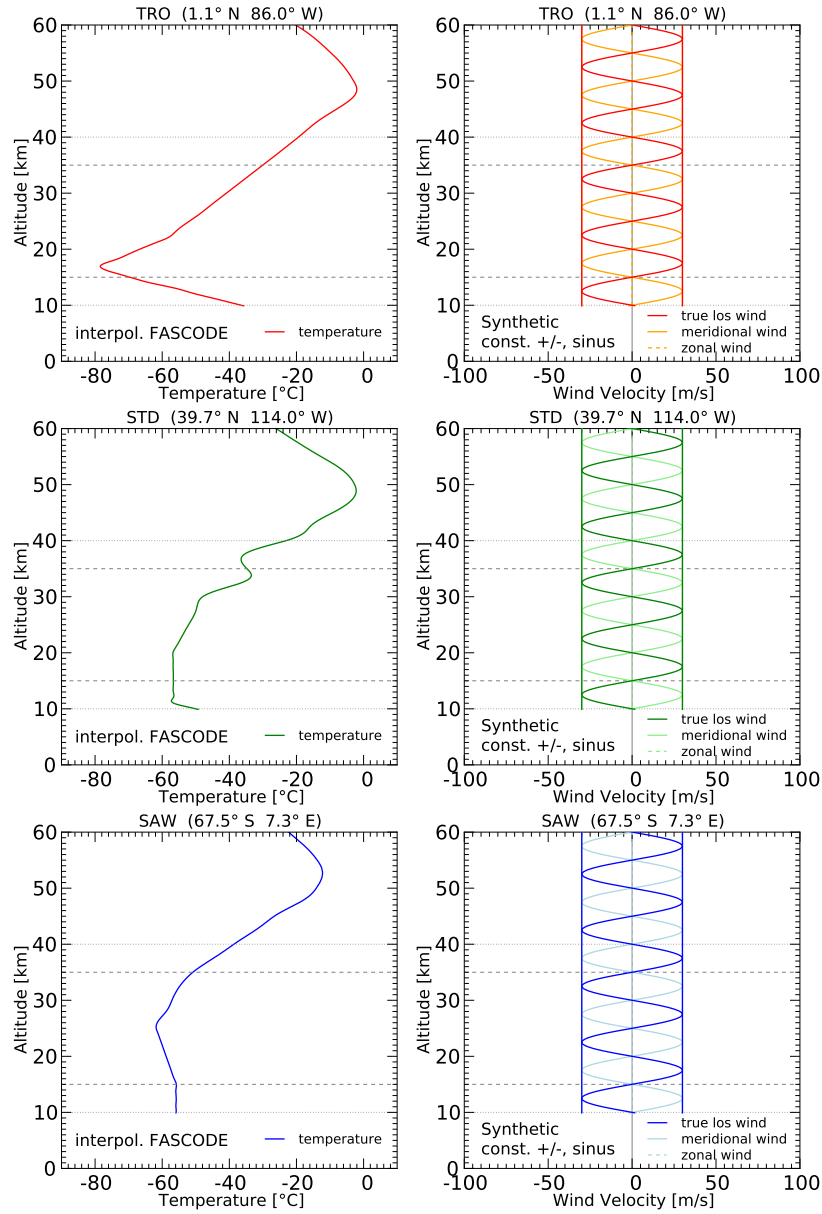


Figure 3.3: Left: Temperature profiles; Right: Meridional, zonal and l.o.s. wind profiles. Temperature profiles interpolated from FASCODE atmosphere. Meridional and zonal wind profiles taken from ECMWF analysis field for all three locations **TRO**, **STD**, **SAW**. **Synthetic wind setup** and **polar orbits** are used. The l.o.s. wind profiles were calculated using xEGOPS tools. Horizontal dashed and dotted lines indicate threshold and target observational requirements, respectively, regarding the altitude range over which the wind retrieval should be usable.

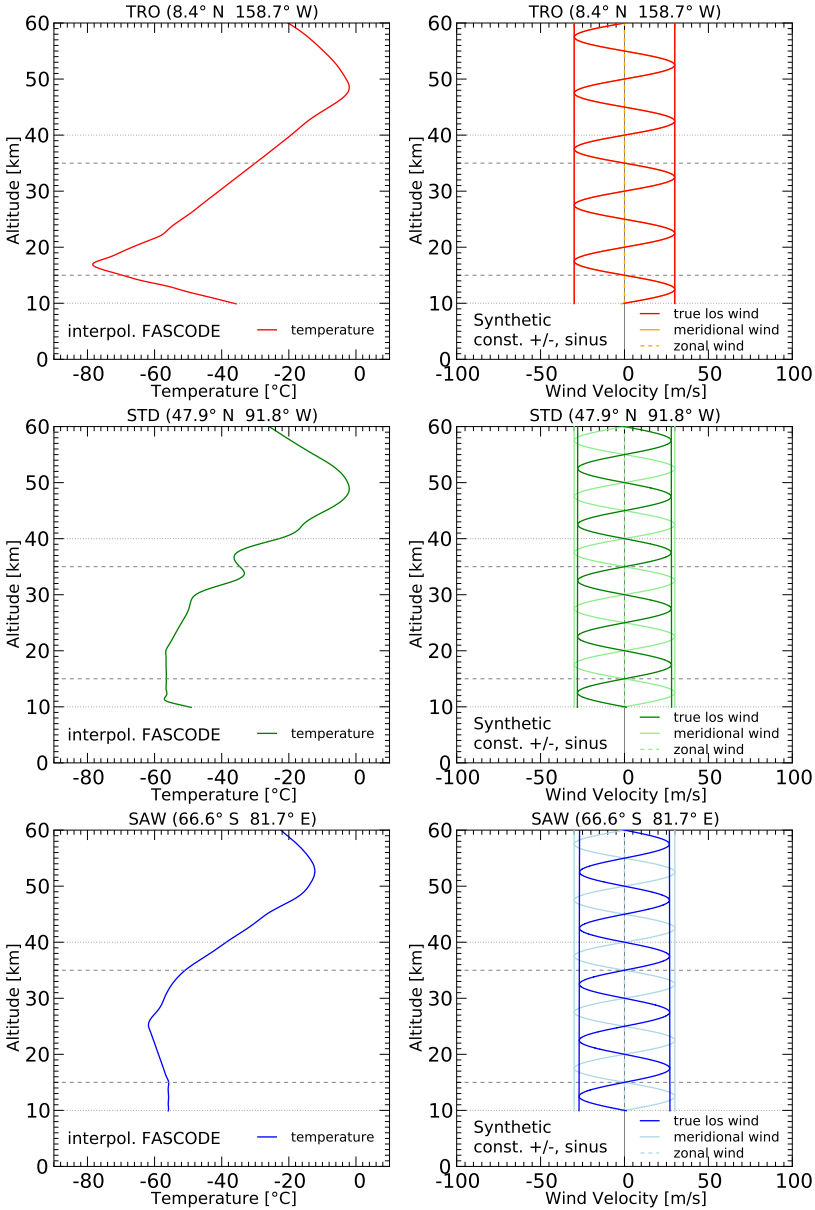


Figure 3.4: Left: Temperature profiles; Right: Meridional, zonal and l.o.s. wind profiles. Temperature profiles interpolated from FASCODE atmosphere. Meridional and zonal wind profiles taken from ECMWF analysis field for all three locations **TRO**, **STD**, **SAW**. **Synthetic wind setup** and **near-polar ($i \approx 80^\circ$) orbits** are used. The l.o.s. wind profiles were calculated using xEGOPS tools. Horizontal dashed and dotted lines indicate threshold and target observational requirements, respectively, regarding the altitude range over which the wind retrieval should be usable.

3 Setup of the Wind Simulations

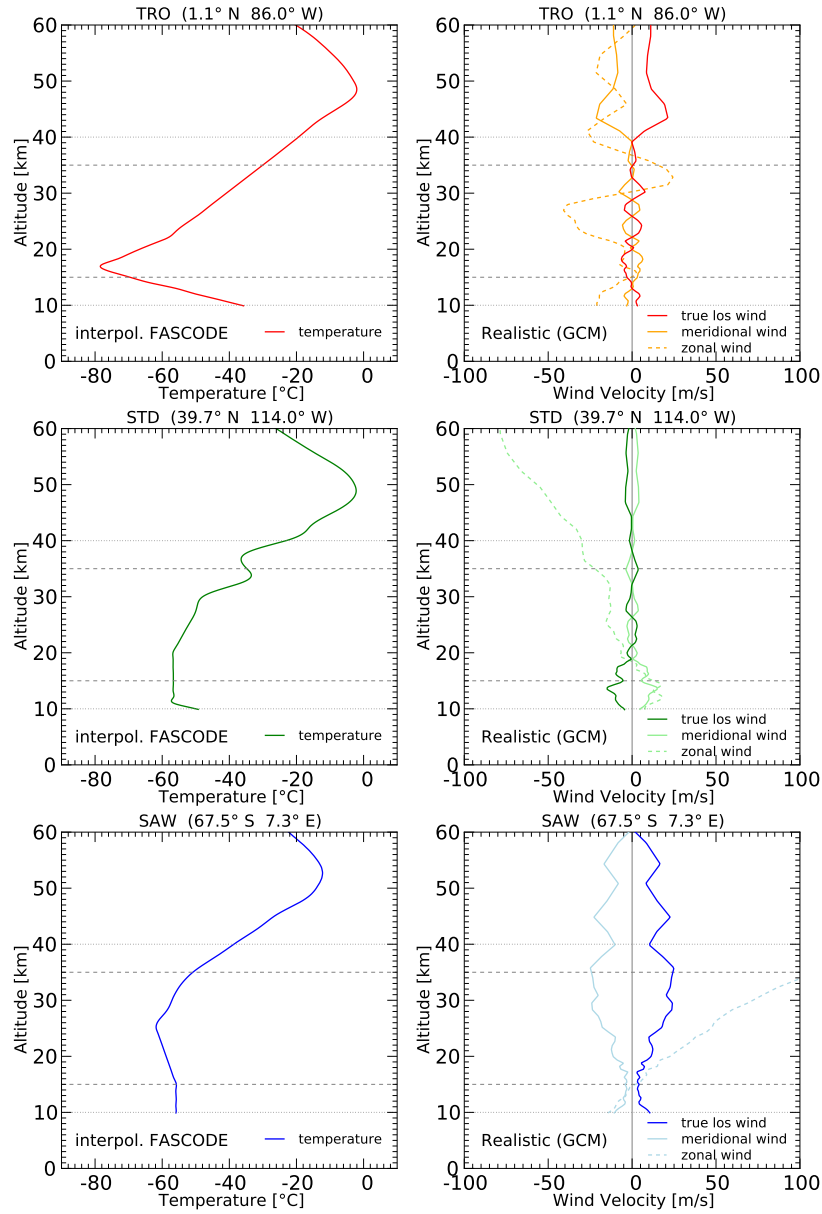


Figure 3.5: Left: Temperature profile; Right: Meridional, zonal and l.o.s. wind profiles. Temperature profiles interpolated from FASCODE atmosphere. Meridional and zonal wind profiles taken from ECMWF analysis field for all three locations **TRO**, **STD**, **SAW**. **Realistic wind setup** and **polar orbits** are used. The l.o.s. wind profiles were calculated using xEGOPS tools. Horizontal dashed and dotted lines indicate threshold and target observational requirements, respectively, regarding the altitude range over which the wind retrieval should be usable.

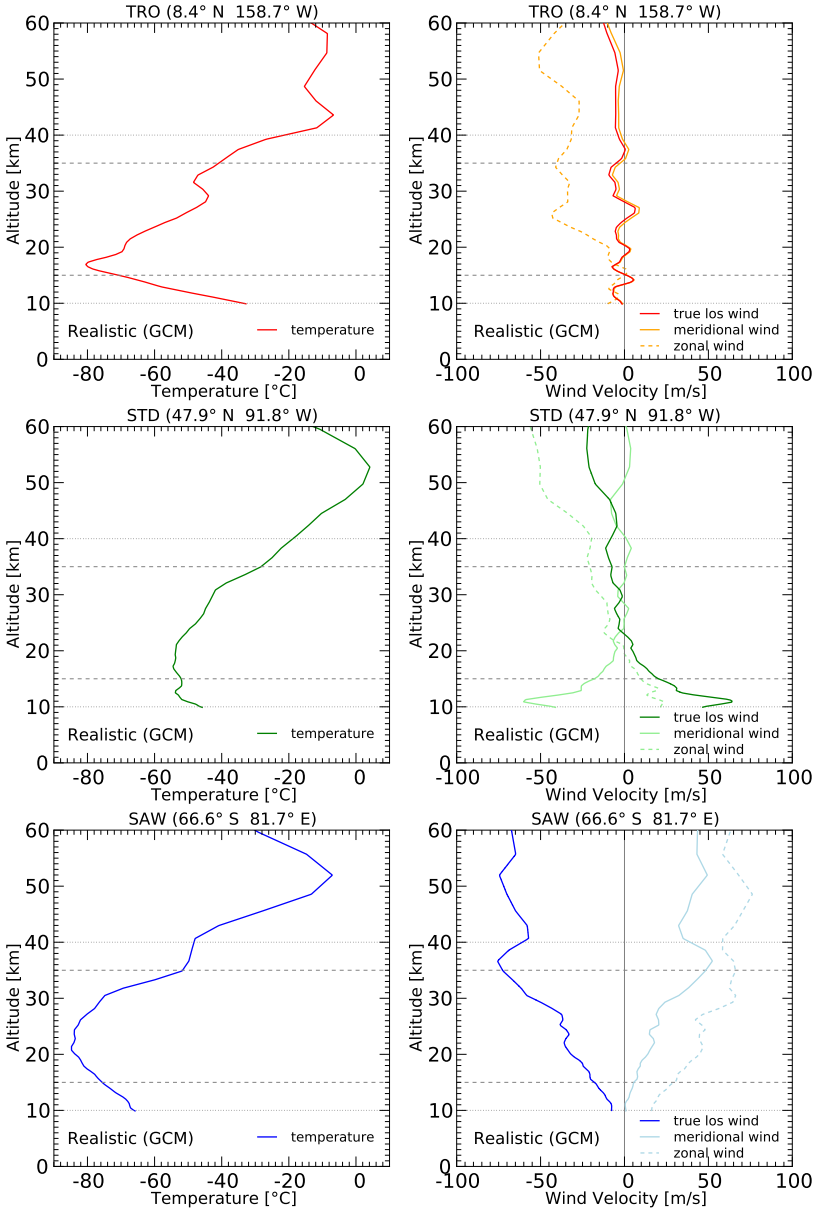


Figure 3.6: Left: Temperature profiles; Right: Meridional, zonal and l.o.s. wind profiles. Temperature profiles and meridional and zonal wind profiles taken from ECMWF analysis field for all three locations **TRO**, **STD**, **SAW**. **Realistic wind setup** and **near-polar ($i \approx 80^\circ$) orbits** are used. The l.o.s. wind profiles were calculated using xEGOPS tools. Horizontal dashed and dotted lines indicate threshold and target observational requirements, respectively, regarding the altitude range over which the wind retrieval should be usable.

4 Wind Retrieval Results

This chapter is presenting the results of the new wind retrieval. A similar discussion is given in Plach et al. (2013). This chapter is similar to Chapter 4 therein.

The chapter starts with an analysis of the general performance of the new wind retrieval in Section 4.1. This is done by using “true” signals without superimposed realistic OSM errors. Next Section 4.2 is dealing with the results for synthetic wind profiles. At the end of the chapter the results for the realistic wind cases are shown.

The discussions, both for synthetic and realistic wind, start with the settings using polar satellite orbits, including a comparison between the simple and the new wind retrieval. This is followed by the near-polar orbit (inclination of $\approx 80^\circ$) settings.

The figures in this chapter all apply the same color scheme. Retrieved values are shown in dark colors, while the “true” values (i.e. $\Delta\Delta T$ from the FOM simulations or “true” l.o.s. wind velocities from the FOM) are indicated in light colors. The three occultation event locations are distinguished by different colors: **TRO**, **STD**, **SAW**.

4.1 General Performance of the new Abel Wind Retrieval

The two types of losses which are considered at the signal attenuation are the Absorption Loss (aLoss) and the Defocusing Loss (dLoss). The aLoss summarizes the processes of target GHG species absorption (here only $C^{18}OO$), absorption of foreign GHG species (for $C^{18}OO$ these are mainly $^{12}CO_2$, $^{13}CO_2$ and H_2O), Rayleigh scattering and aerosol extinction. All extinction loss processes, except the target species absorption, show a very small contribution to the total loss of the selected wind frequencies under investigation here. For further details on these processes and their effects on the IR signal see Schweitzer et al. (2011a).

The magnitudes of aLoss and dLoss can be seen in Figure 4.1. The plot shows the normalized intensity of a IR signal as a function of altitude (exemplary for constant positive wind and polar orbits). Colored lines show the result of signal propagation considering aLoss and dLoss, while in case of the black/gray line only aLoss is taken into account. This is shown for both wind channels, dark colors/black indicating wind channel 1 and light colors/gray wind channel 2.

The IR signal intensity attenuation shows the typical behavior for aLoss and dLoss. The received signal intensity is getting weaker while scanning deeper atmospheric

layers. This is a direct consequence of the higher total atmospheric attenuation in these atmospheric layers, which is mainly governed by increasing densities of all atmospheric species towards the ground. The overall signal evolution, for carbon dioxide, can be seen nicely at the black/gray line, where only aLoss, but no dLoss, was considered. Furthermore the difference between the two channels is evident, it is approximately 0.5 dB. This magnitude corresponds to the figures showing the $\Delta\Delta T$ (e.g. Figure 4.4). Around the tropopause there are some wavy features which can be explained with the dLoss mainly caused by the sharp change in temperature near the tropopause (troposphere to stratosphere), corresponding to a change in refractivity. This discontinuity is representing a barrier for the IR signals (Schweitzer 2010; Schweitzer et al. 2011a).

Figure 4.2 shows the realistic observation error which is superimposed by the OSM, exemplary for constant positive wind and polar orbits. The same color scheme as above is applied. The thermal noise is the dominating factor of the plotted intensity noise. This corresponds to the fact that the SNR decreases with increasing loss and decreasing altitude (Schweitzer 2010). With a smaller SNR the more or less constant thermal noise gets relatively bigger. An imaginative enveloping function reaches a values of approximately ± 0.1 dB near 10 km.

Figure 4.3 is designated to present the basic, or optimal, performance of the new wind retrieval. Exemplary shown for the TRO location and polar orbits. The figure illustrates the retrieval performance under “perfect” conditions. This means that there are no realistic OSM errors superimposed. The left side of the figure gives the retrieved l.o.s. wind (dark colored) in comparison to the true l.o.s. wind (light colored). The corresponding errors are presented on the right side.

The simplest cases of constant winds at the top show very small residual error which are clearly below ± 0.5 m/s. The error of the extreme case of sinusoidal wind (very high wind shear of 60 m/s speed change within 5 km) at the middle right also stays within a maximum of approximately ± 0.5 m/s near the maximum of the sinusoidal wind. Also the retrieval of realistic winds demonstrate a good agreement with the “true” l.o.s. wind speed. The corresponding RMS residual error stays within ± 0.5 m/s. There are only some features which show larger deviations due to the fact that they finite retrieval resolution does not allow the capturing of the “true” feature. Most importantly all the residual errors seem unbiased and the visible fluctuations are merely an expression of the limitations caused by the finite vertical resolution under strongly variable wind. Concluding, it can be stated that the implementation of the new Abel wind retrieval algorithm is numerically robust and accurate.

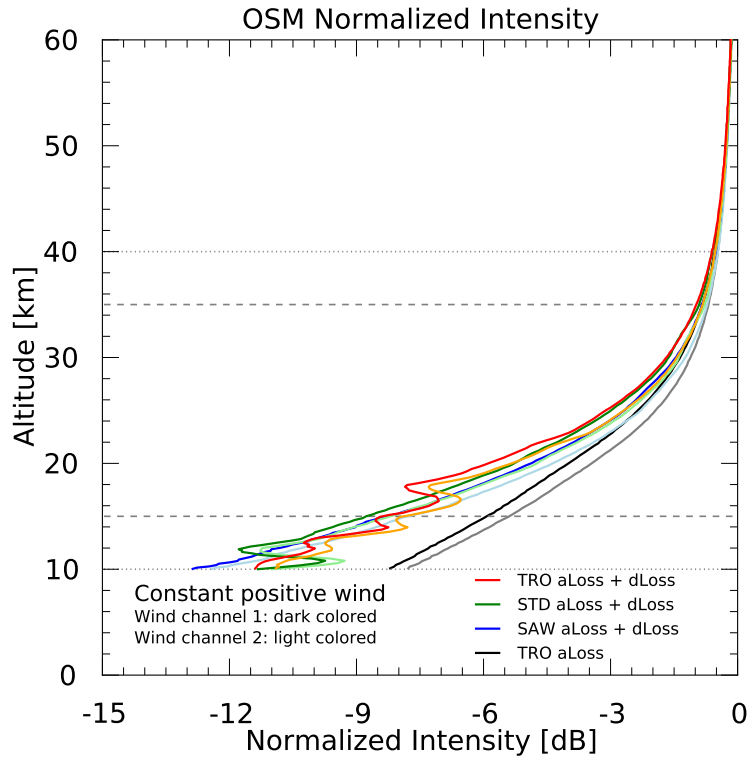


Figure 4.1: OSM normalized intensity loss from absorption (mostly absorption) plus defocusing (TRO, STD, SAW), and extinction only (shown for TRO). Dark colors indicate wind channel 1 and light colors wind channel 2. aLoss stands for absorption (extinction) loss including mainly target greenhouse gas absorption. dLoss is the defocusing loss. The example is from constant positive wind (+30 m/s) and polar orbits. Horizontal dashed and dotted lines indicate threshold and target observational requirements (Kirchengast et al. 2010), respectively, regarding the altitude range over which the wind retrieval should be usable (similar figure in Schweitzer (2010)).

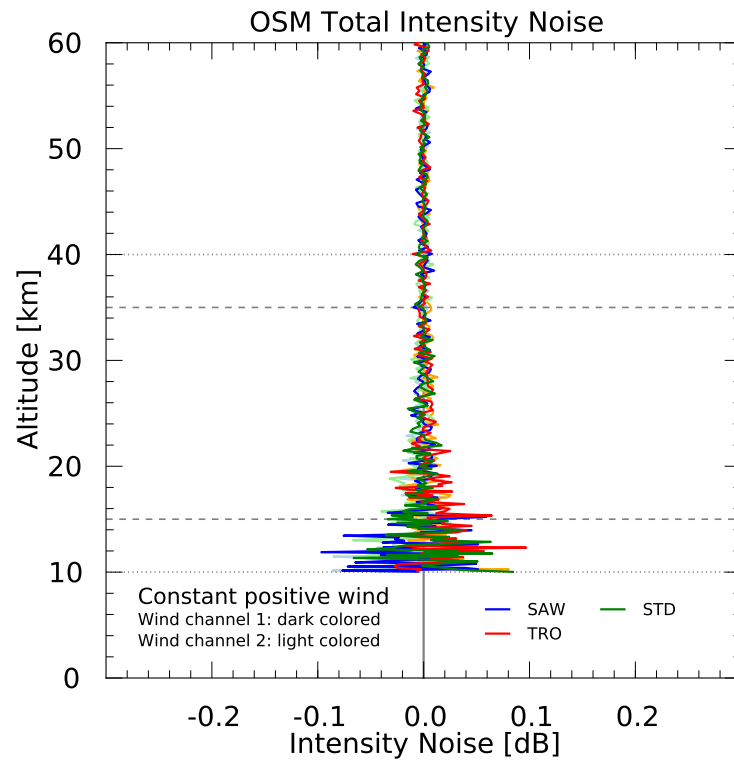


Figure 4.2: Total intensity noise superimposed by the OSM (TRO, STD, SAW). Dark colors indicate wind channel 1 and light colors wind channel 2. Exemplary shown for constant positive wind and polar orbits. Horizontal dashed and dotted lines indicate threshold and target observational requirements (Kirchengast et al. 2010), respectively, regarding the altitude range over which the wind retrieval should be usable (similar figure in Schweitzer (2010)).

4.1 General Performance of the new Abel Wind Retrieval

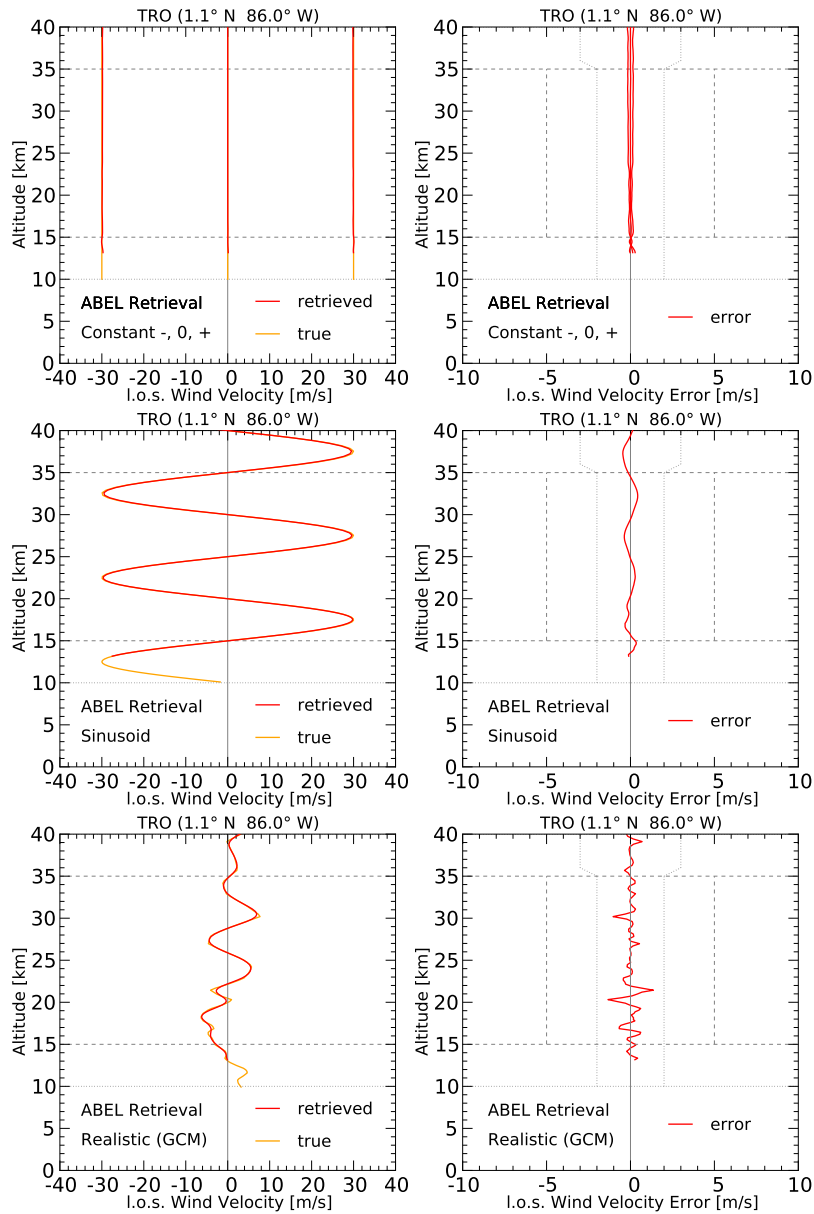


Figure 4.3: l.o.s. wind velocity using a perfect OSM—no observational errors superposed—compared with the “true” l.o.s. wind velocity. The example is showing the **TRO** location and polar orbits. Red lines show the retrieved l.o.s. wind velocity (left) and its error (right). Orange lines indicate the “true” l.o.s. wind velocity. Horizontal dashed and dotted lines indicate threshold and target observational requirements, respectively, regarding the altitude range over which the wind retrieval should be usable. Vertical dashed and dotted lines indicate threshold and target observational requirements, respectively, regarding the wind retrieval accuracy.

4.2 New Wind Retrieval in Synthetic Wind Conditions

This section is presenting the results for the synthetic wind profiles - constant positive (+30 m/s), constant negative (-30 m/s), sinusoidal (± 30 m/s) and no wind. The constant winds and the sinusoidal winds are discussed separately. The setup using polar orbits include a comparison between the new wind retrieval and the older simple wind retrieval (Schweitzer 2010) including OSM errors.

4.2.1 Delta-differential Transmission in Synthetic Wind Conditions

This subsection is taking a closer look at the delta-differential transmission ($\Delta\Delta T$) in synthetic wind conditions, therefore Figure 4.4 and Figure 4.5 are presenting the $\Delta\Delta T$ for every constant and the sinusoidal wind setup using the polar orbits. The $\Delta\Delta T$ is interesting for the comparison since both, the simple and new abel wind, retrievals start with the $\Delta\Delta T$ as their primary input. The preceding preparation steps within the algorithms are basically the same up to this point, including the major preparation steps of correcting the IR tangent point height based on the MW altitude information and the derivation of the transmission for each frequency channel from the measured/simulated amplitudes.

According to the high degree of similarity between the simple and the new wind retrieval algorithm up to here, the $\Delta\Delta T$'s presented in Figure 4.4 and Figure 4.5, are basically identical. The new retrieval on the left and the simple retrieval on the right show the same features, minor differences are a result of minor differences in noise filtering. The two figures confirm that both wind retrieval algorithm use indeed the same input $\Delta\Delta T$ profiles.

For completeness Figure 4.6 and Figure 4.7 show the $\Delta\Delta T$ using the near-polar orbits for all constant and the sinusoidal wind setup. The differences between the forward-modeled "true" $\Delta\Delta T$ (light colored) and the $\Delta\Delta T$ at the start of the OPS, are the superimposed realistic OSM errors. The maximum values for the $\Delta\Delta T$ for the constant positive and constant negative wind setup are a bit smaller than ± 0.5 dB near 17 km. This is in agreement with Figure 4.1, which shows the OSM total intensity noise. The atmospheric influence on the $\Delta\Delta T$, as represented by the superimposed observational noise, is increasing with decreasing altitude.

Especially the figures presenting the constant positive/negative wind setup reveal the changing sensitivity of the wind retrieval with altitude. A larger $\Delta\Delta T$ corresponds to a higher sensitivity of the wind retrieval, since it is the major input. The maximum of the $\Delta\Delta T$ is reached near 19 km, which is a direct consequence of the $C^{18}OO$ absorption line shape. The absorption line has the strongest gradient at the inflexion points at this height (Schweitzer 2010; Kirchengast and Schweitzer 2011).

As expected, a sinusoidal wind profile also results in a sinusoidal alternating $\Delta\Delta T$ profile. The sinusoidal wind profile is simulated with the same maximum and mini-

mum values of ± 30 m/s like the constant positive/negative wind setup. But the corresponding $\Delta\Delta T$ does not reach the same maximum/minimum values, it is damped in dependence of the altitude, which is correctly simulated by the ray-tracking of the FOM module. To get the total attenuation the discrete values at every step along the ray-path are integrated, since the sinusoidal wind field is following local spherical symmetry and therefore is changing sign and magnitude along the way, the total value at the end of the integration can not reach the values of the constant wind cases, where the discrete $\Delta\Delta T$ values are the same in all atmosphere layers.

4 Wind Retrieval Results

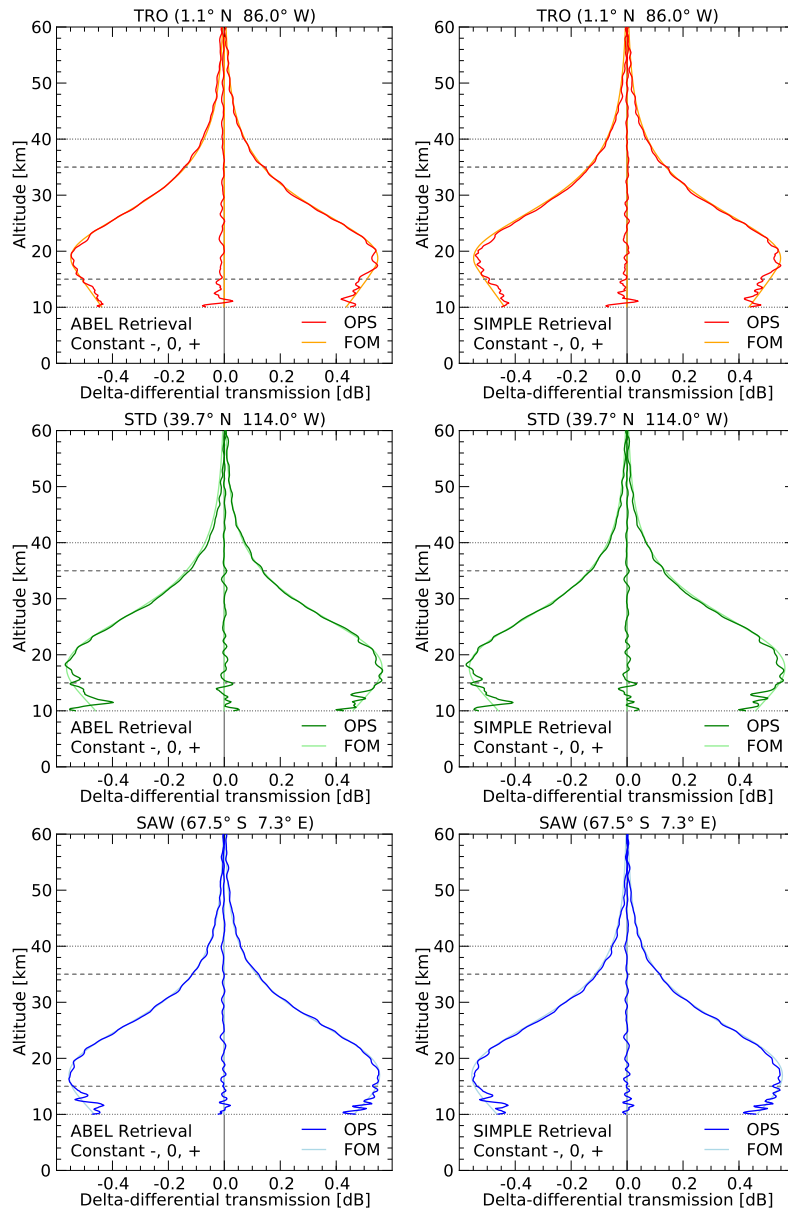


Figure 4.4: Delta-differential transmission ($\Delta\Delta T$) for **all constant wind profiles** using **polar orbits**. New Abel wind retrieval (left) and simple wind retrieval (right). The order of the event locations is from top to bottom: **TRO (red)**, **STD (green)**, **SAW (blue)**. Dark colors indicate the retrieved $\Delta\Delta T$ from OPS, including the superposed OSM errors. Light colors show the “true” $\Delta\Delta T$ from the FOM stage. Horizontal dashed and dotted lines indicate threshold and target observational requirements, respectively, regarding the altitude range over which the wind retrieval should be usable.

4.2 New Wind Retrieval in Synthetic Wind Conditions

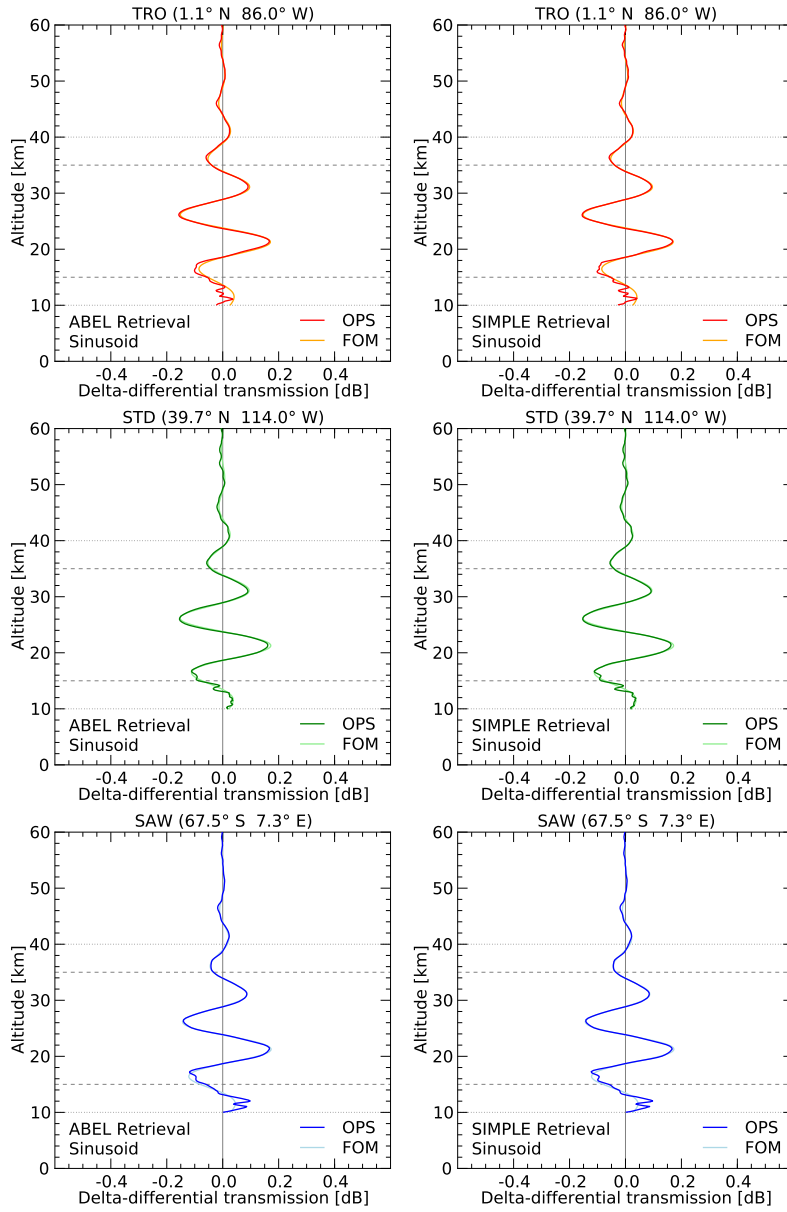


Figure 4.5: Delta-differential transmission ($\Delta\Delta T$) for **sinusoidal wind profiles** using **polar orbits**. New Abel wind retrieval (left) and simple wind retrieval (right). The order of the event locations is from top to bottom: **TRO (red)**, **STD (green)**, **SAW (blue)**. Dark colors indicate the retrieved $\Delta\Delta T$ from OPS, including the superposed OSM errors. Light colors show the “true” $\Delta\Delta T$ from the FOM stage. Horizontal dashed and dotted lines indicate threshold and target observational requirements, respectively, regarding the altitude range over which the wind retrieval should be usable.

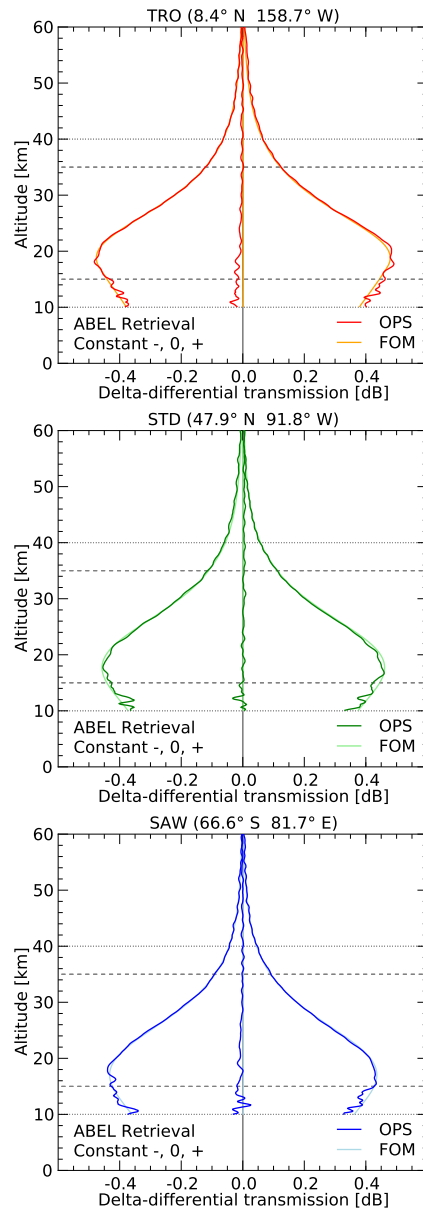


Figure 4.6: Delta-differential transmission ($\Delta\Delta T$) for **all constant wind profiles** using **near-polar ($i \approx 80^\circ$) orbits**. The results for the new Abel wind retrieval are shown. The order of the event locations is (top to bottom): **TRO (red)**, **STD (green)**, **SAW (blue)**. Dark colors indicate the retrieved $\Delta\Delta T$ from the OPS, including the superposed OSM errors. Light colors show the “true” $\Delta\Delta T$ from the FOM stage. Horizontal dashed and dotted lines indicate threshold and target observational requirements, respectively, regarding the altitude range over which the wind retrieval should be usable.

4.2 New Wind Retrieval in Synthetic Wind Conditions

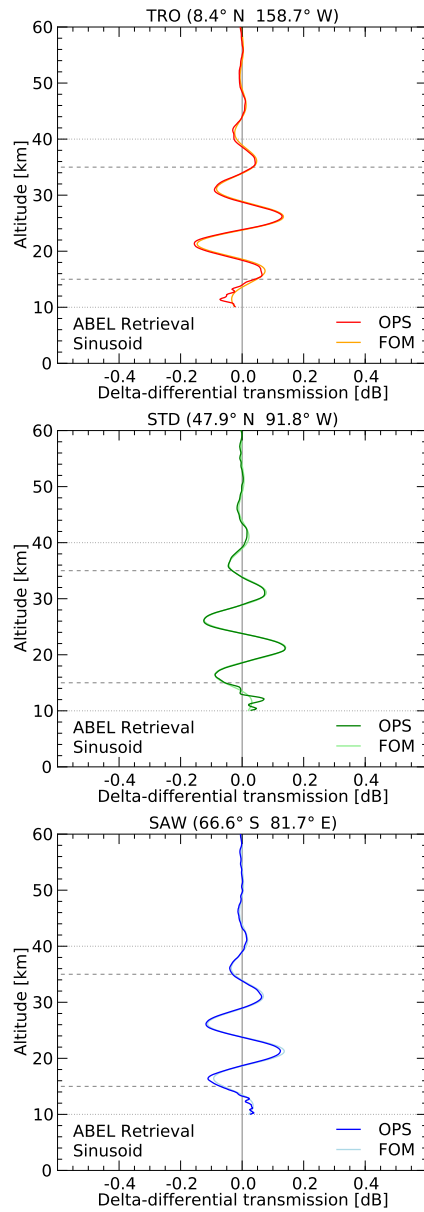


Figure 4.7: Delta-differential transmission ($\Delta\Delta T$) for **sinusoidal wind profiles** using **near-polar ($i \approx 80^\circ$) orbits**. The results for the new Abel wind retrieval are shown. The order of the event locations is (top to bottom): **TRO (red)**, **STD (green)**, **SAW (blue)**. Dark colors indicate the retrieved $\Delta\Delta T$ from the OPS, including the superposed OSM errors. Light colors show the “true” $\Delta\Delta T$ from the FOM stage. Horizontal dashed and dotted lines indicate threshold and target observational requirements, respectively, regarding the altitude range over which the wind retrieval should be usable.

4.2.2 L.o.s. Wind Velocity in Synthetic Wind Conditions

The first l.o.s. wind velocity results are presented in Figure 4.8. The figure shows the outcomes for every constant wind setup for polar orbits including OSM errors. The new Abel wind retrieval is illustrated on the left, while the simple wind retrieval is shown on the right for comparison.

The first thing that can be seen is the higher noise level of the new Abel wind retrieval. This is caused due to the numerical solution of the Abel integral which introduces an error amplification factor of near 2.4 (Kirchengast and Schweitzer 2011; Schweitzer et al. 2011b). While the simple wind retrieval yields wind results close to the true values for every constant wind setup, the retrieved wind from the new wind retrieval show stronger errors.

In more extreme wind conditions, like the sinusoidal wind setup using polar orbits, presented in Figure 4.9, it is obvious that the Abel wind retrieval yields much better results than the simple retrieval. Height-variable wind conditions are the more realistic cases for all practical purposes. Due to the strong wind shear, the simple wind retrieval can not reproduce the sinusoidal wind at all. Besides the decreasing retrieved amplitude with decreasing height, also a phase shift can be seen, since the simple wind retrieval can not properly represent the underlying spherical symmetry of the wind field. For comparison, the Abel wind retrieval exhibits very good agreement with the “true” wind. The only stronger deviation from the *truth* can be observed at the inflection points of the sinusoidal wind profile, which corresponds to a very rapid change in wind direction.

Due to high atmospheric noise and weaker SNR in the lower atmospheric layers, all retrieved wind profiles are cut off at 13 km, since the wind retrievals no longer show any useful results below this point.

The retrieval results for the synthetic wind profiles and near-polar orbits are quite similar. They are presented in Figure 4.10 and Figure 4.11. As discussed above (Section 3.4) the l.o.s. wind (for near-polar orbits) is depending on the latitude of the occultation event. Since the ± 30 m/s meridional component is projected into the near-polar orbit occultation plane the l.o.s. wind speeds are somewhat reduced towards higher latitudes. Corresponding to this, the TRO events are almost perfectly meridional, the SAW events on the other hand show clearly reduced wind speeds. The retrieved l.o.s. winds for the SAW cases exhibit maximum values of around ± 27 m/s opposite to ± 30 m/s for polar orbits.

4.2 New Wind Retrieval in Synthetic Wind Conditions

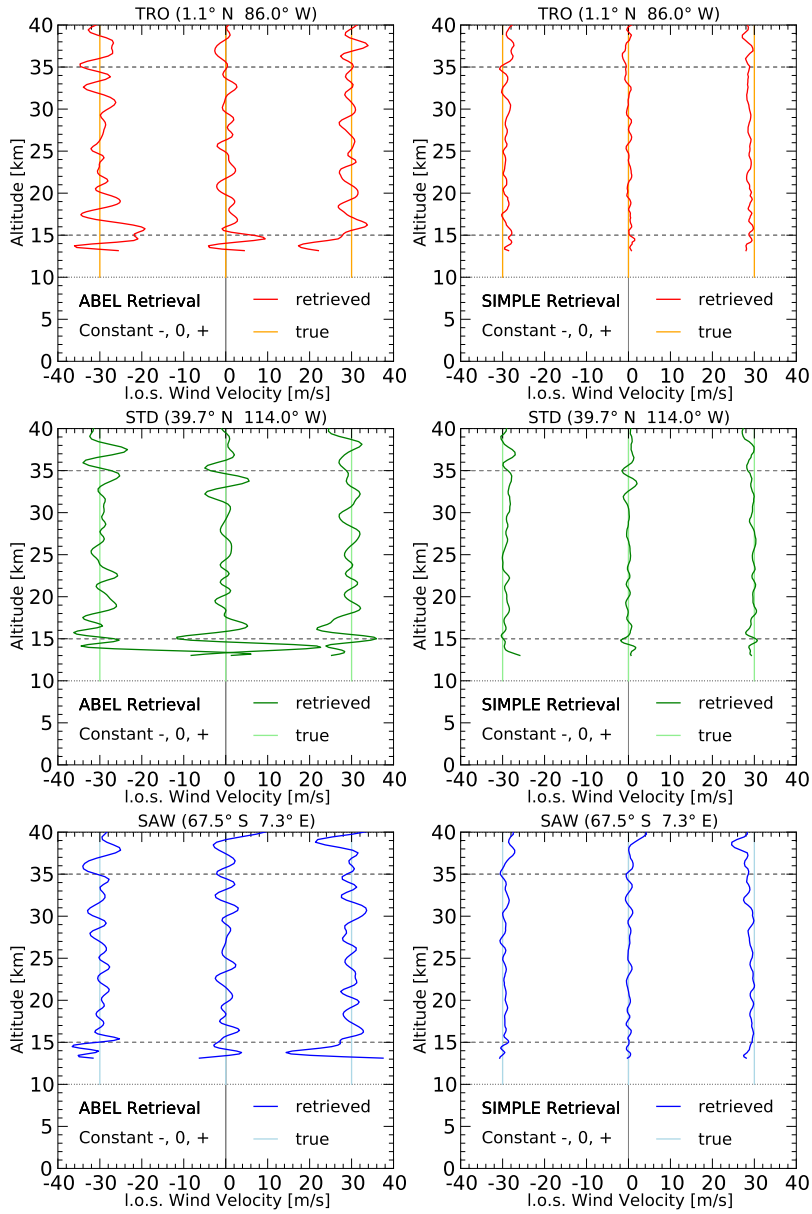


Figure 4.8: l.o.s. wind velocity for all constant wind profiles using polar orbits. New Abel wind retrieval (left) and simple wind retrieval (right). The order of the event locations is (top to bottom): TRO (red), STD (green), SAW (blue). Dark colors indicate the retrieved l.o.s. wind velocity from the OPS while light colors show the "true" wind velocity from the FOM. Horizontal dashed and dotted lines indicate threshold and target observational requirements, respectively, regarding the altitude range over which the wind retrieval should be usable.

4 Wind Retrieval Results

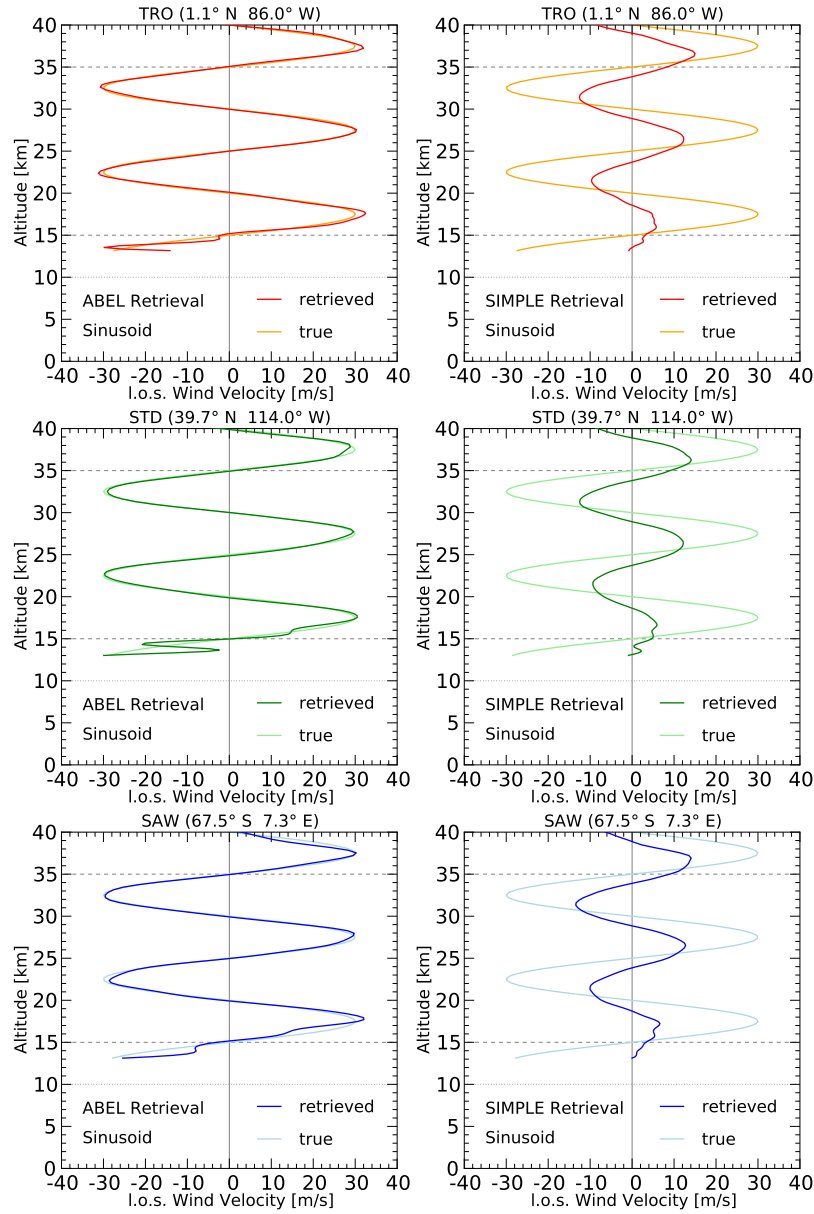


Figure 4.9: l.o.s. wind velocity for **sinusoidal wind profiles** using **polar orbits**. New Abel wind retrieval (left) and simple wind retrieval (right). The order of the event locations is (top to bottom): **TRO (red)**, **STD (green)**, **SAW (blue)**. Dark colors indicate the retrieved l.o.s. wind velocity from the OPS while light colors show the "true" wind velocity from the FOM. Horizontal dashed and dotted lines indicate threshold and target observational requirements, respectively, regarding the altitude range over which the wind retrieval should be usable.

4.2 New Wind Retrieval in Synthetic Wind Conditions

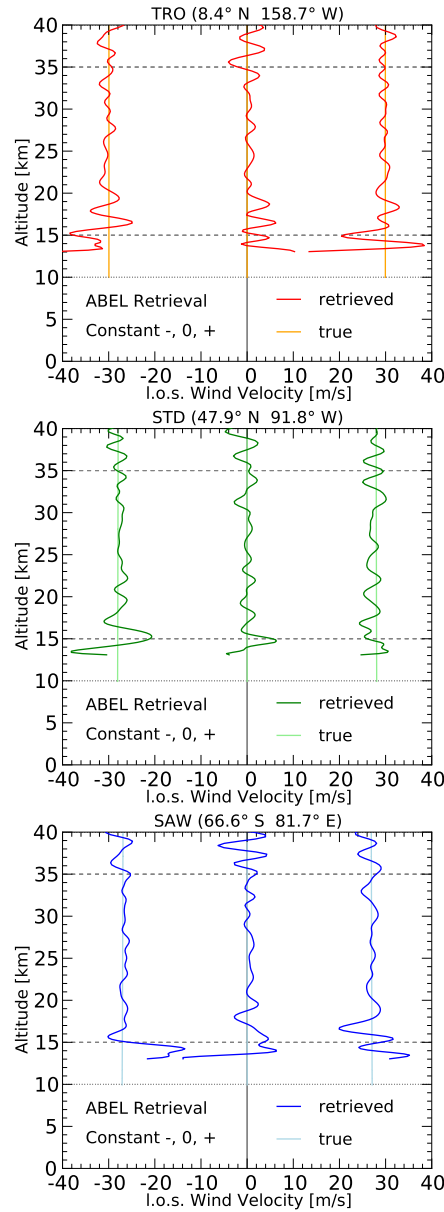


Figure 4.10: l.o.s. wind velocity for **all constant wind profiles** using **near-polar** ($i \approx 80^\circ$) **orbits**. The results for the new Abel wind retrieval are shown. The order of the event locations is (top to bottom): **TRO** (red), **STD** (green), **SAW** (blue). Dark colors indicate the retrieved l.o.s. wind velocity from the OPS, light colors show the "true" l.o.s. wind velocity from the FOM. Horizontal dashed and dotted lines indicate threshold and target observational requirements, respectively, regarding the altitude range over which the wind retrieval should be usable.

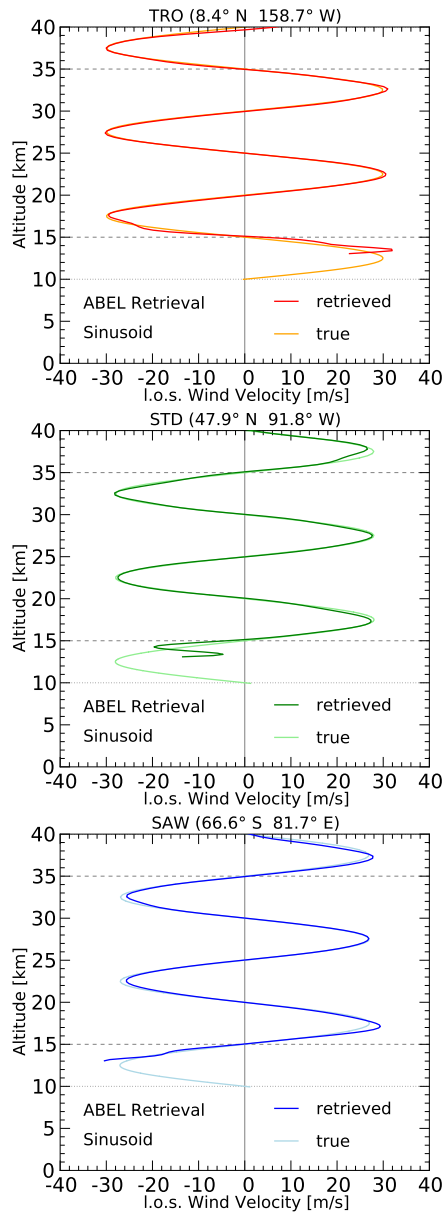


Figure 4.11: l.o.s. wind velocity for **sinusoidal wind profiles** using **near-polar ($i \approx 80^\circ$) orbits**. The results for the new Abel wind retrieval are shown. The order of the event locations is (top to bottom): **TRO (red)**, **STD (green)**, **SAW (blue)**. Dark colors indicate the retrieved l.o.s. wind velocity from the OPS, light colors show the "true" l.o.s. wind velocity from the FOM. Horizontal dashed and dotted lines indicate threshold and target observational requirements, respectively, regarding the altitude range over which the wind retrieval should be usable.

4.2.3 L.o.s. Wind Velocity Error in Synthetic Wind Conditions

This subsection is presenting the retrieval errors of the l.o.s. wind velocity. In Figure 4.12 the single profile errors for every constant wind setup with polar orbits are plotted in thin lines. In addition the moving average (averaging over ± 2 km at each altitude) and its standard deviation are shown in bold red and black, respectively. Due to the low number of samples these parameters are only an estimate for the bias and the statistical error. Again the left side is showing the new wind retrieval and the right side the simple retrieval for reference. The estimated mean stays within ± 0.5 m/s for the altitude range from 15 to 35 km, suggesting basically unbiased results. The estimated standard error lays between ± 2.0 m/s (target requirement) from 17 to 35 km for the Abel retrieval and even more clearly within these requirements for the simple retrieval since these are just synthetic constant winds. Comparing the two retrievals the already mentioned error amplification caused by the Abel integral (Kirchengast and Schweitzer 2011) can be seen quite nicely.

Figure 4.13 is presenting the errors for the sinusoidal cases with polar orbits. It shows a similar picture for the Abel retrieval (left panel), but the estimated mean also has a sinusoidal pattern, since the strong wind shear at the inflection points of the wind profile cause larger errors. But the sinusoidal variations of the wind can be reproduced. As discussed before the simple retrieval (right panel) can not derive any usable wind results for the sinusoidal case, since it is unable to deal with the strongly height-variable wind conditions.

The retrieval errors for the new Abel wind retrieval using near-polar orbits are illustrated in Figure 4.14 and Figure 4.15 showing constant winds and sinusoidal winds, respectively. These results are showing a similar behavior compared to the corresponding polar-orbit results, and thus again demonstrating the robustness and basic reliability of the new Abel wind retrieval.

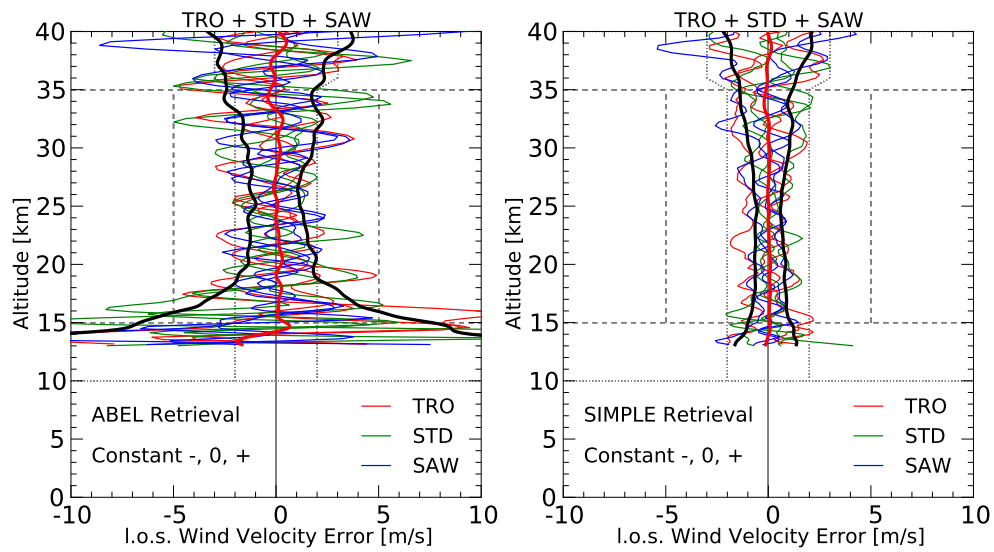


Figure 4.12: l.o.s. wind velocity error for **all constant wind profiles** using **polar orbits**. Results from the new Abel retrieval (left) and the simple wind retrieval (right). The light lines show the l.o.s. wind velocity error for single profiles. The heavy red line indicates the moving average (mean), from averaging at each altitude over an adjacent range of ± 2 km. The heavy black lines show the corresponding standard deviation estimates. Horizontal dashed and dotted lines indicate threshold and target observational requirements, respectively, regarding the altitude range over which the wind retrieval should be usable. Vertical dashed and dotted lines indicate threshold and target observational requirements, respectively, regarding the retrieval accuracy.

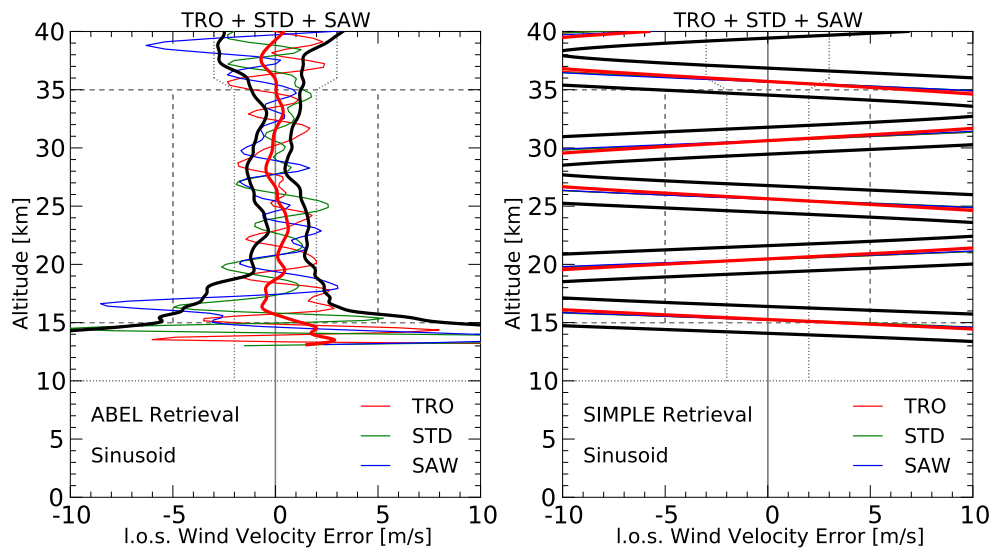


Figure 4.13: l.o.s. wind velocity error for **sinusoidal wind profiles** using **polar orbits**. Results from the new Abel retrieval (left) and the simple wind retrieval (right). The light lines show the l.o.s. wind velocity error for single profiles. The heavy red line indicates the moving average (mean), from averaging at each altitude over an adjacent range of ± 2 km. The heavy black lines show the corresponding standard deviation estimates. Horizontal dashed and dotted lines indicate threshold and target observational requirements, respectively, regarding the altitude range over which the wind retrieval should be usable. Vertical dashed and dotted lines indicate threshold and target observational requirements, respectively, regarding the retrieval accuracy.

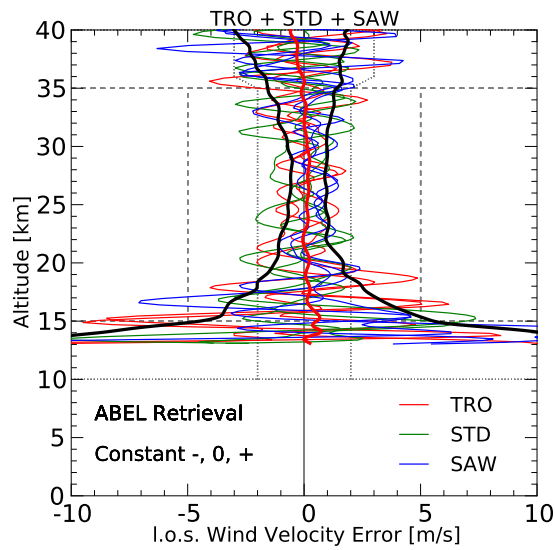


Figure 4.14: l.o.s. wind velocity error for **all constant wind profiles** using **near-polar** ($i \approx 80^\circ$) **orbits**. Results from the new Abel retrieval are shown. The light lines show the l.o.s. wind velocity error for single profiles. The heavy red line indicates the moving average (mean), from averaging at each altitude over an adjacent range of ± 2 km. The heavy black lines show the corresponding standard deviation estimates. Horizontal dashed and dotted lines indicate threshold and target observational requirements, respectively, regarding the altitude range over which the wind retrieval should be usable. Vertical dashed and dotted lines indicate threshold and target observational requirements, respectively, regarding the retrieval accuracy.

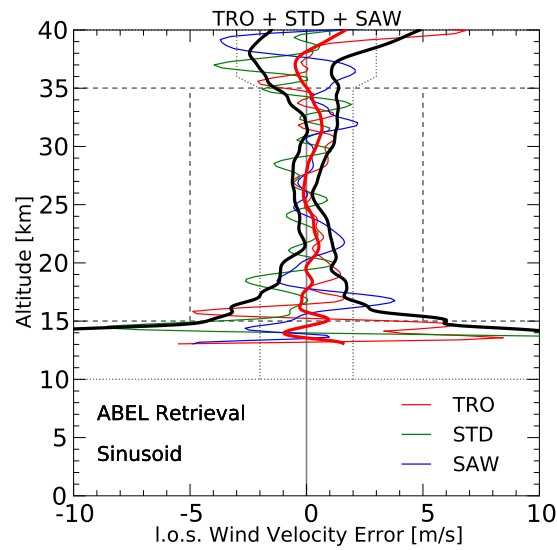


Figure 4.15: l.o.s. wind velocity error for **sinusoidal wind profiles** using **near-polar** ($i \approx 80^\circ$) **orbits**. Results from the new Abel retrieval are shown. The light lines show the l.o.s. wind velocity error for single profiles. The heavy red line indicates the moving average (mean), from averaging at each altitude over an adjacent range of ± 2 km. The heavy black lines show the corresponding standard deviation estimates. Horizontal dashed and dotted lines indicate threshold and target observational requirements, respectively, regarding the altitude range over which the wind retrieval should be usable. Vertical dashed and dotted lines indicate threshold and target observational requirements, respectively, regarding the retrieval accuracy.

4.3 New Wind Retrieval in Realistic Wind Conditions

This section is discussing the delta-differential transmission ($\Delta\Delta T$), the l.o.s. wind velocity and the corresponding error for realistic wind conditions in the same fashion as it is done in the preceding section for the synthetic wind conditions.

4.3.1 Delta-differential Transmission in Realistic Wind Conditions

The $\Delta\Delta T$ for realistic wind conditions is shown in Figure 4.16 and Figure 4.17 for polar and for near-polar orbits, respectively. Similar to Subsection 4.2.1 this section shows that the two wind retrievals start with almost identical inputs ($\Delta\Delta T$ profiles).

The values of the $\Delta\Delta T$ are generally much smaller for these realistic cases, since geographic locations with sustained meridional wind speeds of 30 m/s or more (used speeds in the synthetic cases) are hard to find in reality in the investigated altitude range up to 40 km. The SAW events are the exception here. They reach up to 0.25 dB and 0.7 dB, respectively, corresponding with high meridional wind speeds.

Once more all retrieved $\Delta\Delta T$ profiles are in good agreement with the “true” forward-modeled ones. The noise levels are again higher in lower atmosphere layers, mainly due to the decrease of the SNR with the near-exponential increase of species densities in the lower atmosphere.

4.3 New Wind Retrieval in Realistic Wind Conditions

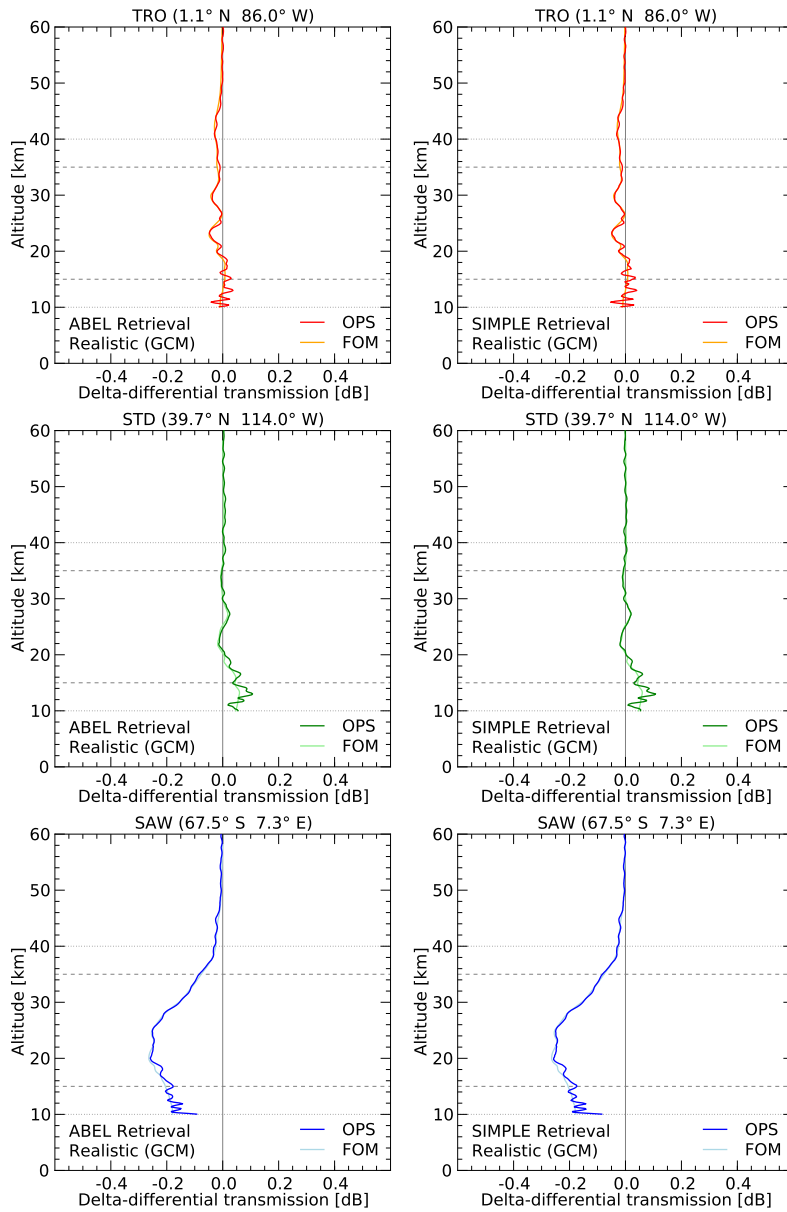


Figure 4.16: Delta-differential transmission ($\Delta\Delta T$) for **realistic wind profiles** using **polar orbits**. New Abel wind retrieval (left) and simple wind retrieval (right). The order of the event locations is (top to bottom): **TRO (red)**, **STD (green)**, **SAW (blue)**. Dark colors indicate the retrieved $\Delta\Delta T$ from the OPS, including the superposed OSM errors. Light colors show the "true" $\Delta\Delta T$ from the FOM stage. Horizontal dashed and dotted lines indicate threshold and target observational requirements, respectively, regarding the altitude range over which the wind retrieval should be usable.

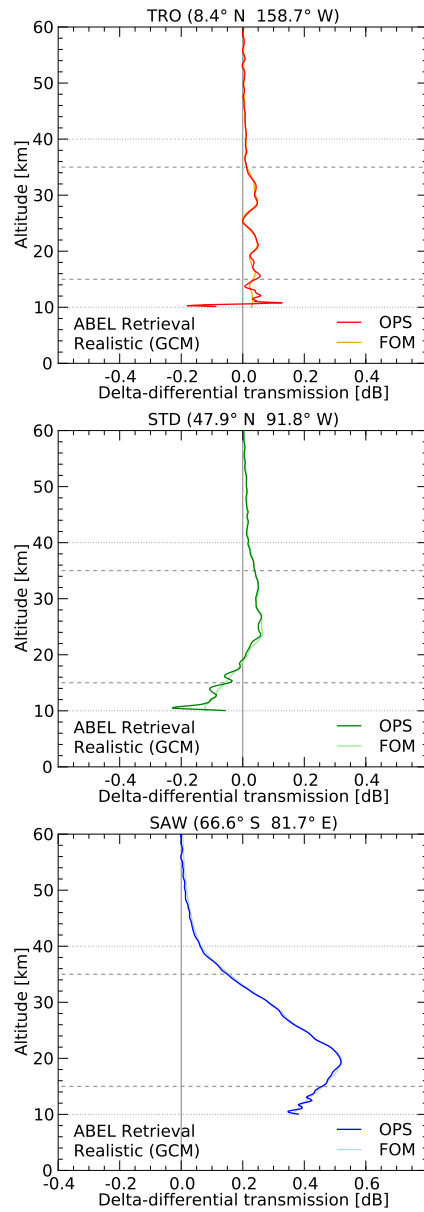


Figure 4.17: Delta-differential transmission ($\Delta\Delta T$) for **realistic wind profiles** using **near-polar ($i \approx 80^\circ$) orbits**. Results for the new Abel wind retrieval are shown. The order of the event locations is (top to bottom): **TRO (red)**, **STD (green)**, **SAW (blue)**. Dark colors indicate the retrieved $\Delta\Delta T$ from the OPS, including the superposed OSM errors. Light colors show the "true" $\Delta\Delta T$ from the FOM stage. Horizontal dashed and dotted lines indicate threshold and target observational requirements, respectively, regarding the altitude range over which the wind retrieval should be usable.

4.3.2 L.o.s. Wind Velocity in Realistic Wind Conditions

Figure 4.18 clarifies that the new wind retrieval can also handle realistic wind velocity quite well. There is a good agreement between the retrieved and the “true” l.o.s. wind down to about 17 km. Below 20 km the error increases in particular for lower l.o.s. wind speeds and more humid atmosphere since the SNR for the $\Delta\Delta T$ of these cases is decreasing and thus the system reaches the internal l.o.s. wind resolution boundary.

The simple wind retrieval to the contrary shows major deviations at all altitude levels due to the inability of correctly retrieving height-variable winds.

The l.o.s. wind velocities for the near-polar orbits presented in Figure 4.19 show that the realistic cases at all three locations are retrieved reliably again. There is also an example for an extreme wind speed maximum at the SAW location. It is demonstrated that also a high l.o.s. wind speed maximum of 75 m/s in the upper stratosphere can be retrieved in a satisfactory fashion, showing the high dynamic range for reliable retrievals.

4 Wind Retrieval Results

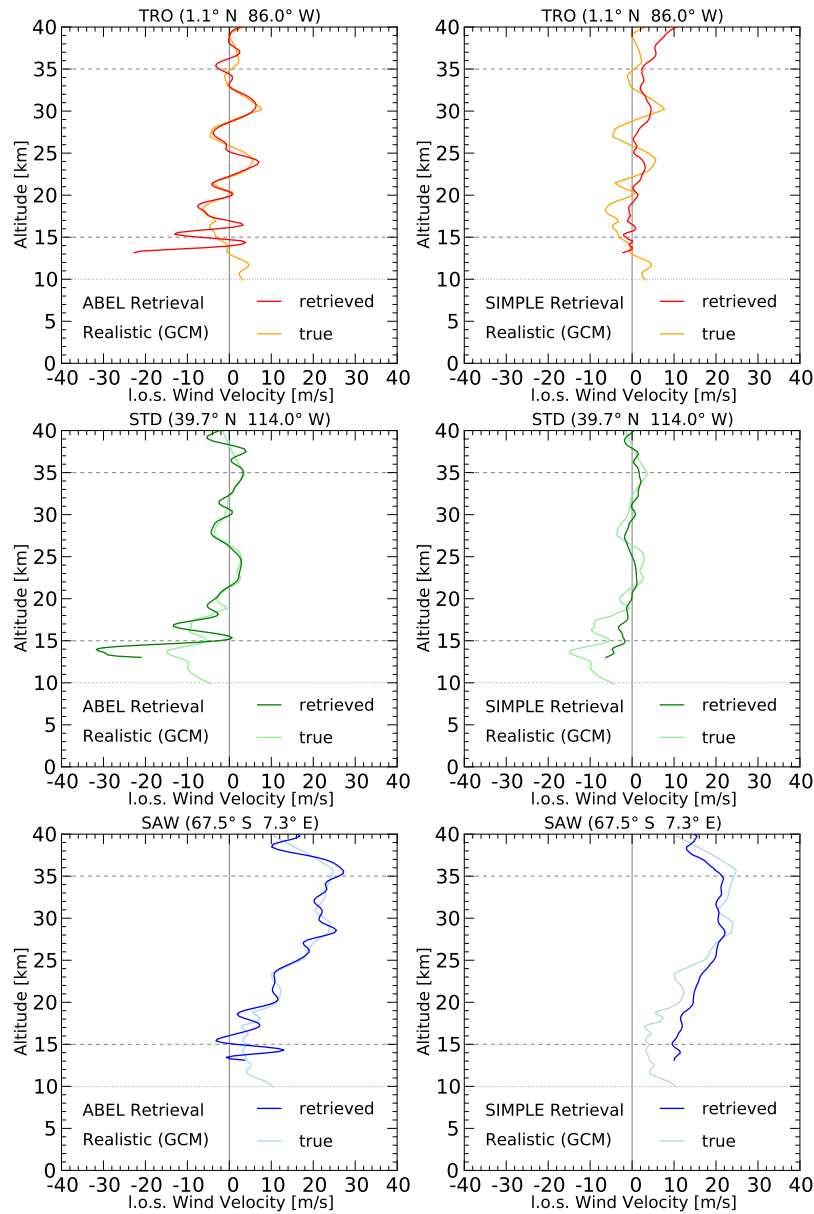


Figure 4.18: l.o.s. wind velocity for **realistic wind profiles** using **polar orbits**. New Abel wind retrieval (left) and simple wind retrieval (right). The order of the event locations is (top to bottom): **TRO (red)**, **STD (green)**, **SAW (blue)**. Dark colors indicate the retrieved l.o.s. wind velocity from the OPS while light colors show the "true" wind velocity from the FOM. Horizontal dashed and dotted lines indicate threshold and target observational requirements, respectively, regarding the altitude range over which the wind retrieval should be usable.

4.3 New Wind Retrieval in Realistic Wind Conditions

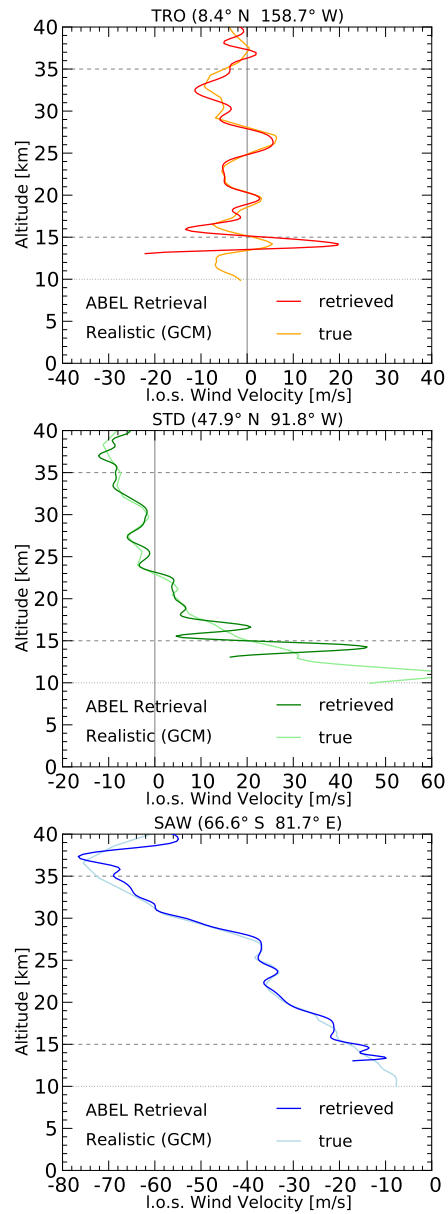


Figure 4.19: l.o.s. wind velocity for realistic wind profiles using near-polar ($i \approx 80^\circ$) orbits. The results for the new Abel wind retrieval are shown. The order of the event locations is (top to bottom): **TRO** (red), **STD** (green), **SAW** (blue). Dark colors indicate the retrieved l.o.s. wind velocity from the OPS, light colors show the "true" l.o.s. wind velocity from the FOM. Horizontal dashed and dotted lines indicate threshold and target observational requirements, respectively, regarding the altitude range over which the wind retrieval should be usable.

4.3.3 L.o.s. Wind Velocity Error in Realistic Wind Conditions

The final results are presented in this section. Figure 4.20 and Figure 4.21 show the l.o.s. wind velocity errors for realistic wind conditions for polar and near-polar orbits, respectively. The error plots follow the same scheme as in Subsection 4.2.3. The new Abel wind errors show a estimated mean within $\pm 1\text{m/s}$ down to 17 km, again indicating essentially unbiased retrievals. The standard deviation estimates and the corresponding single error profiles stay within $\pm 2\text{m/s}$ from 35 km down to below 20 km. Below 20 km they start to diverge, but stay within the threshold requirements down to near 15 km. As the SNR is dropping in the troposphere also the noise starts to increase accordingly. Overall the results for the new Abel wind retrieval are promising a reliable derivation of l.o.s. wind speeds in the stratosphere above 15 km.

The errors for the simple wind retrieval in contrary show strong mean errors, indicating strongly biased results over extended height ranges exceeding the target requirements already. Furthermore, the standard deviation estimate of the simple retrieval is not fulfilling the target requirements at any height level. This leads to the conclusion that the simple wind retrieval is not a practical option for reliable wind retrieval under realistic conditions.

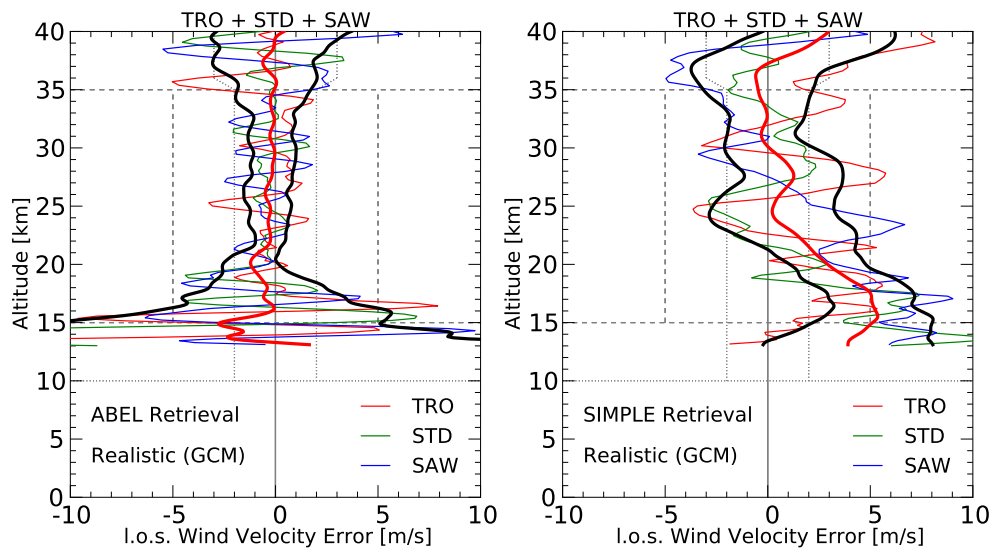


Figure 4.20: l.o.s. wind velocity error for **realistic wind profiles** using **polar orbits**. Results from the new Abel retrieval (left) and the simple wind retrieval (right). The light lines show the l.o.s. wind velocity error for single profiles. The heavy red line indicates the moving average (mean), from averaging at each altitude over an adjacent range of ± 2 km. The heavy black lines show the corresponding standard deviation estimates. Horizontal dashed and dotted lines indicate threshold and target observational requirements, respectively, regarding the altitude range over which the wind retrieval should be usable. Vertical dashed and dotted lines indicate threshold and target observational requirements, respectively, regarding the retrieval accuracy.

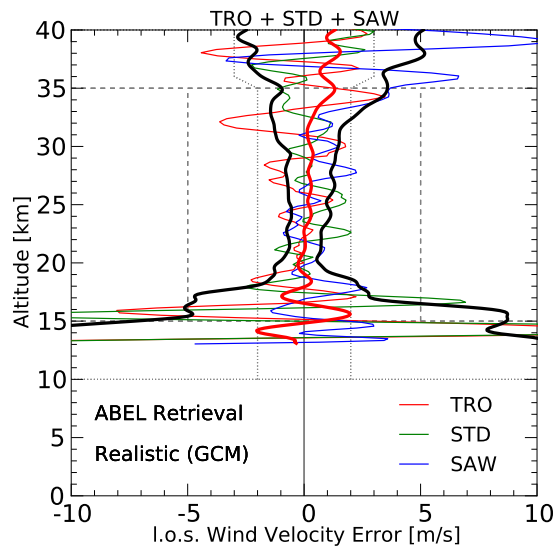


Figure 4.21: l.o.s. wind velocity error for **realistic wind profiles** using **near-polar** ($i \approx 80^\circ$) **orbits**. Results for the new Abel retrieval are shown. The light lines show the l.o.s. wind velocity error for single profiles. The heavy red line indicates the moving average (mean), from averaging at each altitude over an adjacent range of ± 2 km. The heavy black lines show the corresponding standard deviation estimates. Horizontal dashed and dotted lines indicate threshold and target observational requirements, respectively, regarding the altitude range over which the wind retrieval should be usable. Vertical dashed and dotted lines indicate threshold and target observational requirements, respectively, regarding the retrieval accuracy.

Summary and Conclusion

A *new algorithm for wind profiling* of the atmosphere from LIO measurements was introduced in this thesis. It is embedded and uses preparatory steps from the GHG retrieval algorithm from IR signals in clear air (Proschek et al. 2011b). The new wind algorithm is based on an Abel transform derived by Syndergaard and Kirchengast (2013). Its implementation in the xEGOPS software package is explained in detail. Results of end-to-end simulations are shown to demonstrate the capability of the new algorithm.

Within these end-to-end simulations synthetic and realistic wind profiles are investigated. The synthetic profiles represent a vertically constant positive (+30 m/s), a vertically constant negative (−30 m/s), a sinusoidal alternating (± 30 m/s) and no wind. The realistic wind profiles are taken from an ECMWF analysis field. All these wind profiles are analyzed for two sets of satellite orbits and three geographic locations.

The two sets of satellite orbits differ mainly in their inclination. One using a polar inclination of exactly 90° and the other a near-polar inclination of $\approx 80^\circ$, representing the most recent orbits for a future satellite mission (Kirchengast et al. 2010). The three geographic locations represent three different atmospheric conditions. A warm and moist atmosphere from the tropics - TRO, an intermediate atmosphere from mid-latitudes - STD, and a cold and dry atmosphere from around the southern polar circle - SAW. The thermodynamic state variables corresponding to these atmospheric conditions are mostly taken from the FASCODE atmosphere (FASCODE 2008). Only for the realistic wind profiles and the near-polar orbits, the thermodynamic state variables are taken from the ECMWF analysis field. The necessary GHG concentrations are always provided by the FASCODE atmosphere.

A performance review is done by comparing the retrieved and the true input wind profiles and by analyzing the corresponding retrieval errors yielded from the difference of the two. There is also a comparison to the formerly used *simple wind retrieval* (Schweitzer 2010), for the polar orbit setup, included in the performance review.

The results show that the new Abel wind retrieval, in contrast to the simple wind retrieval, is working well in strongly height-variable winds (sinusoidal) and in high speed winds (SAW cases). The retrieved mean wind is found to be essentially unbiased; the mean wind retrieval errors stay within ± 0.5 m/s. The corresponding standard deviation lays within the target requirement of ± 2 m/s over the altitude

range from about 17 km up to 35 km. This applies even though the Abel transform is introducing a noise amplification (Kirchengast and Schweitzer 2011; Schweitzer et al. 2011b) compared to the simple retrieval. The new Abel wind retrieval is also working well in fairly extreme conditions, like the discussed sinusoidal wind profiles, with vertical changes of 60 m/s over 5 km, and the realistic ECMWF-derived wind conditions.

Furthermore it is shown that the simple wind retrieval only shows good performance for (synthetic) height-constant winds, but is not capable of retrieving realistic and sinusoidal wind profiles in a reliable manner, because it is not able to derive height-varying wind profiles.

To summarize, the outcome is reinforcing the evidence that the new Abel wind retrieval can be an asset to the LMIO method within the ACCURATE mission concept (Kirchengast and Schweitzer 2011). Besides the need for precise wind profiles themselves, they can also be used to account for the wind-induced Doppler shift of the absorption line frequencies which are used in the GHG retrieval from IR signals.

In the future this wind correction will help reduce the residual error and therefore also provide accurate GHG profiles in windy air. First steps for implementation of the wind correction are already in place and the preliminary results are encouraging.

List of Figures

1.1	Schematic overview of the LMIO geometry	7
1.2	Transmission spectrum and its first derivative of the absorption line	9
2.1	Basic LMIO algorithm scheme	14
2.2	Illustration of spherically symmetric wind velocity	16
2.3	Wind algorithm in retrieval scheme	20
3.1	Global occultation of events, polar orbits	29
3.2	Global occultation of events, near-polar ($i \approx 80^\circ$) orbits	30
3.3	Temperature and wind profiles for synthetic wind setup and polar orbits	32
3.4	Temperature and wind profiles for synthetic wind setup and near-polar ($i \approx 80^\circ$) orbits	33
3.5	Temperature and wind profiles for realistic wind setup and polar orbits	34
3.6	Temperature and wind profiles for realistic wind setup and near-polar ($i \approx 80^\circ$) orbits	35
4.1	OSM intensity with and without defocusing loss	39
4.2	OSM total intensity noise	40
4.3	Perfect OSM wind retrieval	41
4.4	Delta-differential transmission, all constant winds, polar orbits . . .	44
4.5	Delta-differential transmission, sinusoidal wind, polar orbits	45
4.6	Delta-differential transmission, all constant winds, near-polar ($i \approx 80^\circ$) orbits	46
4.7	Delta-differential transmission, sinusoidal winds, near-polar ($i \approx 80^\circ$) orbits	47
4.8	L.o.s. wind velocity, all constant winds, polar orbits	49
4.9	L.o.s. wind velocity, sinusoidal wind, polar orbits	50
4.10	l.o.s. wind velocity, all constant winds, near-polar ($i \approx 80^\circ$) orbits .	51
4.11	l.o.s. wind velocity, sinusoidal wind, near-polar ($i \approx 80^\circ$) orbits . .	52
4.12	l.o.s. wind velocity error, all constant winds, polar orbits	54
4.13	l.o.s. wind velocity error, sinusoidal wind, polar orbits	55
4.14	l.o.s. wind velocity error, all constant winds, near-polar ($i \approx 80^\circ$) orbits	56
4.15	l.o.s. wind velocity error, sinusoidal wind, near-polar ($i \approx 80^\circ$) orbits	57

List of Figures

4.16	Delta-differential transmission, realistic wind, polar orbits	59
4.17	Delta-differential transmission, realistic wind, near-polar ($i \approx 80^\circ$) orbits	60
4.18	l.o.s. wind velocity, realistic wind, polar orbits	62
4.19	l.o.s. wind velocity, realistic wind, near-polar ($i \approx 80^\circ$) orbits	63
4.20	l.o.s. wind velocity error, realistic winds, polar orbits	65
4.21	l.o.s. wind velocity error, realistic winds, near-polar ($i \approx 80^\circ$) orbits	66

List of Tables

3.1	Settings for the RX and TX using polar orbits	25
3.2	Settings for the RX and TX using near-polar ($i \approx 80^\circ$) orbits	25
3.3	Atmosphere and forward simulation settings	26
3.4	OSM Instrumental errors for LIO RX and TX	26
3.5	OSM Instrumental errors for LMO RX and TX	27
3.6	Absorption and reference channels - polar orbits (HITRAN 2004).	28
3.7	Absorption and reference channels - near-polar orbits (HITRAN 2008).	28

Bibliography

- Anderson, G. P., S. A. Clough, F. X. Kneizys, J. H. Chetwynd, and E. P. Shettle (1986). *AFGL atmospheric constituent profiles (0–120km)*. Environm. Res. Papers, Tech. Rep. 954, AFGL-TR-86-0110. Hanscom AFB, Massachusetts, USA: Optical Phys. Div., Air Force Geophys. Lab.
- Bönsch, G. and E. Potulski (1998). “Measurements of the refractive index of air and comparison with modified Edlén’s formulae.” *Metrologia* 35, pp. 133–139.
- Dudhia, A. (2008). *Reference Forward Model RFM*. Inst. of Atmos., Oceanic and Planet. Phys., Univ. of Oxford, Oxford, UK. URL: <http://www.atm.ox.ac.uk/RFM/>.
- Edwards, D. P. (1996). *High level algorithm definition document*. Tech. Rep. ESA/ESTEC PO-TN-OXF-GS-0004, Contract No. 11886/96/NL/GS. Oxford, United Kingdom: Inst. of Atmos., Oceanic and Planet. Phys., Univ. of Oxford. URL: <http://www.atm.ox.ac.uk/RFM/>.
- ESA (2004). *ACE+ Atmosphere and Climate Explorer. Technical and Programmatic Annex*. European Space Agency Specification Publication, ESA SP-1279(4), 1–39. Available at <http://esamultimedia.esa.int/docs/EEUCM/ACE+TPA.pdf>.
- FASCODE (2008). *cited 2008 on RFM website - FASCODE model atmospheres*. Inst. of Atmos., Oceanic and Planet. Phys., Univ. of Oxford, Oxford, UK. URL: <http://www.atm.ox.ac.uk/RFM/atm>.
- Fritzer, J. M., G. Kirchengast, and M. Pock (2009). *End-to-End Generic Occultation Performance Simulation and Processing System version 5.5 (EGOPS 5.5) Software User Manual*. Tech. Rep. ESA–ESTEC WEGC–EGOPS–2009–TR01. Version 1. Graz, Austria: Wegener Center and Inst. for Geophys., Astrophys., and Meteorol., Univ. of Graz.
- Fritzer, J. M., G. Kirchengast, M. Pock, and V. Proschek (2010). *End-to-End Generic Occultation Performance Simulation and Processing System version 5.5 (EGOPS 5.5 and xEGOPS) Software User Manual*. Tech. Rep. ESA–ESTEC WEGC–EGOPS–2010–TR01. Version 1. Graz, Austria: Wegener Center and Inst. for Geophys., Astrophys., and Meteorol., Univ. of Graz.

- Gorbunov, M. E. and G. Kirchengast (2005). "Processing X/K band radio occultation data in the presence of turbulence." *Radio Sci.* 40, RS6001. DOI: 10.1029/2005RS003263.
- Gorbunov, M. E. and G. Kirchengast (2007). "Fluctuations of radio occultation signals in X/K band in the presence of anisotropic turbulence and differential transmission retrieval performance." *Radio Sci.* 42, RS4025. DOI: 10.1029/2006RS003544.
- Healy, S. (2013). *Use of GNSS Radio Occultation Data in NWP at ECMWF*. Presentation held at the OPAC-IROWG 2013 (Seggau Castle, Austria) in September 2013.
- Herman, B. M., D. Feng, D. Flittner, E. R. Kursinski, S. Syndergard, and D. Ward (2004). "An overview of the University of Arizona ATMOS project." In: *Occultations for Probing Atmosphere and Climate*. Ed. by G. Kirchengast, U. Foelsche, and A. K. Steiner. Berlin-Heidelberg: Springer Verlag.
- Ho, S.-P., G. Kirchengast, S. Lero, J. Wickert, A. J. Mannuci, A. K. Steiner, D. Hunt, W. Schreiner, S. Sokolovskiy, C. Ao, M. W. Borsche, A. von Engeln, U. Foelsche, S. Heise, B. Lijima, Y.-H. Kuo, E. R. Kursinski, B. Pirscher, M. Ringer, C. Rocken, and T. Schmidt (2009). "Estimating the uncertainty of using GPS radio occultation data for climate monitoring: Inter-comparison of CHAMP refractivity climate records 2002–2006 from different data centers." *J. Geophys. Res.* 114, D23107. DOI: 10.1029/2009JD011969.
- Kirchengast, G. (2004). "Occultations for probing atmosphere and climate: setting the scene." In: *Occultations for Probing Atmosphere and Climate*. Ed. by G. Kirchengast, U. Foelsche, and A. K. Steiner. Berlin-Heidelberg: Springer Verlag.
- Kirchengast, G. and P. Hoeg (2004). "The ACE+ mission: An atmosphere and climate explorer based on GPS, GALILEO and LEO-LEO radio occultation." In: *Occultations for Probing Atmosphere and Climate*. Ed. by G. Kirchengast, U. Foelsche, and A. K. Steiner. Berlin-Heidelberg: Springer Verlag.
- Kirchengast, G. and S. Schweitzer (2007). *ACCURATE LEO-LEO Infrared Laser Occultation Initial Assessment: Requirements, Payload Characteristics, Scientific Performance Analysis, and Breadboarding Specifications*. Tech. Rep. FFG-ALR No. 03/2007. Graz, Austria: Wegener Center, Univ. of Graz.
- Kirchengast, G. and S. Schweitzer (2011). "Climate benchmark profiling of greenhouse gases and thermodynamic structure and wind from space." *Geophys. Res. Lett.* 38.13, L13701. DOI: doi:10.1029/2011GL047617.

- Kirchengast, G., P. F. Bernath, S. Buehler, G. Durry, L. Facheris, C. Gerbig, L. Haimberger, J. Harris, A. Hauchecorne, E. Kurölä, G. B. Larsen, R. Sausen, R. A. Anthes, M. E. Gorbunov, E. R. Kursinski, S. S. Leroy, K. Trenberth, B. Randel, J. Gille, and T. Tsuda (2010). *ACCURATE—climate benchmark profiling of greenhouse gases and thermodynamic variables and wind from space (ESA Earth Explorer Opportunity Mission EE-8 proposal)*. Sci. Rep. No. 36, document wcv-scirep-no36-gkirchengastetal-jul2010.pdf. Graz, Austria: Wegener Center Verlag. URL: <http://www.wegcenter.at/wcv>.
- Kursinski, E. R., G. A. Hajj, J. T. Schofield, R. P. Linfield, and K. R. Hardy (1997). “Observing Earth’s atmosphere with radio occultation measurements using the global positioning system.” *J. Geophys. Res.* 102.D19, pp. 23429–23465.
- Kursinski, E. R., S. Syndergaard, D. Flittner, D. Feng, G. Hajj, B. Herman, D. Ward, and T. Yunck (2002). “A microwave occultation observing system optimized to characterize atmospheric water, temperature and geopotential via absorption.” *J. Atmos. Ocean. Tech.* 19, pp. 1897–1914. DOI: 10.1175/1520-0426(2002)019.
- Kursinski, E. R., D. Ward, A. Otarola, K. Frehlich, C. Groppi, S. Albanna, M. Shein, W. Bertiger, H. Pickett, and M. Ross (2009). “The Active Temperature, Ozone and Moisture Microwave Spectrometer (ATOMMS).” In: *New Horizons in Occultation Research*. Ed. by A. K. Steiner, B. Pirscher, U. Foelsche, and G. Kirchengast. Berlin-Heidelberg: Springer Verlag. DOI: 10.1007/978-3-642-00321-9_24.
- Phinney, R. A. and D. L. Anderson (1968). “On the radio occultation method for studying planetary atmospheres.” *J. Geophys. Res.* 73.5, pp. 1819–1827. DOI: 10.1029/JA073i005p01819.
- Plach, A., V. Proschek, and G. Kirchengast (2013). *Abel transform retrieval of wind profiles from LEO-LEO IR laser occultation: End-to-end simulations and performance analysis*. Tech. Rep. for ESA/ESTEC No. 2/2013 AEXPWIND TN3—Part2. Graz, Austria: Wegener Center, Univ. of Graz.
- Proschek, V., S. Schweitzer, and G. Kirchengast (2011a). *Greenhouse Gas Profiles Retrieval from IR-laser Occultation Data in Cloudy Air*. Tech. Rep. for FFG-ALR No. 1/2011. Graz, Austria: Wegener Center, Univ. of Graz.
- Proschek, V., G. Kirchengast, and S. Schweitzer (2011b). “Greenhouse gas profiling by infrared-laser and microwave occultation: retrieval algorithm and demonstration results from end-to-end simulations.” *Atmos. Meas. Tech.* 4.10, pp. 2035–2058. DOI: 10.5194/amt-4-2035-2011.

- Rothman, L. S., D. Jacquemart, A. Barbe, D. Chris Benner, M. Birk, L. R. Brown, M. R. Carleer, C. Chackerian Jr., K. Chance, L. H. Coudert, V. Dana, V. M. Devi, J.-M. Flaud, R. R. Gamache, A. Goldman, et al. (2005). “The HITRAN 2004 molecular spectroscopic database.” *J. Quantitat. Spectrosc. Radiat. Transf.* 96.2, pp. 139–204. DOI: 10.1016/j.jqsrt.2004.10.008.
- Rothman, L. S. et al. (2009). “The HITRAN 2008 molecular spectroscopic database.” *J. Quantitat. Spectrosc. Radiat. Transf.* 110.9–10, pp. 533–572. DOI: 10.1016/j.jqsrt.2009.02.013.
- Schweitzer, S. (2010). *The ACCURATE concept and the infrared laser occultation technique: Mission design and assessment of retrieval performance (Ph.D. thesis)*. Sci. Rep. No. 34, document wcv-scirep-no34-sschweitzer-jun2010.pdf. Graz, Austria: Wegener Center Verlag. URL: <http://www.wegcenter.at/wcv>.
- Schweitzer, S., G. Kirchengast, and V. Proschek (2011a). “Atmospheric influences on infrared-laser signals used for occultation measurements between Low Earth Orbit satellites.” *Atmos. Meas. Tech.* 4.10, pp. 2273–2292. DOI: 10.5194/amt-4-2273-2011.
- Schweitzer, S., G. Kirchengast, M. Schwärz, J. M. Fritzer, and M. E. Gorbunov (2011b). “Thermodynamic state retrieval from microwave occultation data and performance analysis based on end-to-end simulations.” *J. Geophys. Res.* 116, D10301. DOI: 10.1029/2010JD014850.
- Steiner, A. K., G. Kirchengast, B. Pirscher, M. W. Borsche, and U. Foelsche (2009). “Atmospheric temperature change detection with GPS radio occultation 1995 to 2008.” *Geophys. Res. Lett.* 36, L18702. DOI: 10.1029/2009GL039777.
- Steiner, A. K., B. C. Lackner, F. H. Ladstädter, B. Scherllin-Pirscher, U. Foelsche, and G. Kirchengast (2011). “GPS Radio Occultation for Climate Monitoring and Change Detection.” *Radio Sci.* 46, RS0D24. DOI: 10.1029/2010RS004614.
- Steiner, A. K., D. Hunt, S.-P. Ho, G. Kirchengast, A. J. Mannucci, B. Scherllin-Pirscher, H. Gleisner, A. von Engeln, T. Schmidt, C. Ao, S. S. Leroy, E. R. Kursinski, U. Foelsche, M. Gorbunov, S. Heise, Y.-H. Kuo, K. B. Lauritsen, C. Marquardt, C. Rocken, W. Schreiner, S. Sokolovskiy, S. Syndergaard, and J. Wickert (2013). “Quantification of structural uncertainty in climate data records from GPS radio occultation.” *Atmos. Chem. Phys.* 13.3, pp. 1469–1484. DOI: 10.5194/acp-13-1469-2013.
- Syndergaard, S. and G. Kirchengast (2013). *Formulation and analysis of an Abel transform for deriving line-of-sight wind profiles from LEO-LEO IR laser occultation*. Tech. Rep. for ESA/ESTEC No. 1/2013 AEXPWIND TN3—Part1. Graz, Austria: Wegener Center, Univ. of Graz.

- Thayer, G. D. (1974). "An improved equation for the radio refractive index of air." *Radio Sci.* 9, pp. 803–807.
- Ware, R., M. Exner, D. Feng, M. E. Gorbunov, K. Hardy, B. M. Herman, W. Kuo, T. Meehan, W. Melbourne, C. Rocken, W. Schreiner, S. Sokolovskiy, F. Solheim, X. Zou, R. Anthes, S. Businger, and K. Trenberth (1996). "GPS sounding of the atmosphere from low Earth orbit: Preliminary results." *Bull. Amer. Meteorol. Soc.* 77, pp. 19–40.

Abstract:

The Low Earth Orbit (LEO) mission concept of LEO–LEO Microwave and Infrared-laser Occultation (LMIO) has the goal of providing climate benchmark profiles of Greenhouse Gases (GHGs), thermodynamic variables and line-of-sight (l.o.s.) wind from space with focus on the Upper Troposphere–Lower Stratosphere (UTLS) region (5 km to 35 km) as an independent, self-calibrating, and active remote limb-sounding measurement concept.

So far only a so called simple wind retrieval algorithm, which assumes a constant wind velocity over the entire occultation ray path, was investigated within LMIO. Here the implementation and results of a new and advanced wind retrieval algorithm are shown. It uses the more accurate assumption that the wind velocity is spherically symmetric within the UTLS. Therefore the wind can be retrieved by using an Abel Transform. The differential transmission principle is applied to two wind-sensitive absorption channels to minimize atmospheric broadband effects. The measured frequency shifts are proportional to the wind-induced Doppler shift.

The performance of the new algorithm is examined with end-to-end simulations. Synthetic and realistic l.o.s. wind profiles in three greatly different geographic regions are investigated. Furthermore two sets of satellite orbits, polar and near-polar, are analyzed. The results show that the new wind retrieval is capable of deriving the l.o.s. wind speed in an approximate altitude range from 15 to 35 km, where it also works for highly variable wind profiles and high speed winds.

Zum Inhalt:

Das Low Earth Orbit (LEO) Missionskonzept der LEO-LEO Microwave and Infrared-laser Occultation (LMIO) hat das Ziel der Gewinnung von Profilen für Treibhausgase (THG), thermodynamische Zustandsvariablen und line-of-sight (l.o.s.) Wind von Satelliten aus, als unabhängiges, selbstkalibrierendes und aktives Limb-Sounding Messkonzept. Dabei liegt der Fokus auf der oberen Troposphäre und der unteren Stratosphäre (UTLS) (5 km bis 35 km).

Bisher wurde nur ein einfacher Wind-Retrieval Algorithmus innerhalb LMIO untersucht. Dieser benutzt die Annahme einer konstanten Windgeschwindigkeit entlang des gesamten Okkultations-Strahlweges. Hier werden die Implementierung und die Ergebnisse für einen neuen und fortgeschrittenen Wind-Retrieval Algorithmus diskutiert. Dieser verwendet die genauere Annahme, dass die Windgeschwindigkeit in der UTLS sphärisch symmetrisch ist, daher kann der Wind über eine Abel-Transformation gewonnen werden. Das Differenzielle Transmissionsprinzip wird auf zwei Wind-Absorptionslinien angewandt, um atmosphärische Breitband-Effekte zu minimieren. Die gemessenen Frequenzverschiebungen sind proportional zur windinduzierten Dopplerverschiebung.

Die Leistungsfähigkeit des neuen Retrievals wird im Zuge von End-to-end Simulationen für synthetische und realistische l.o.s. Windprofile in drei stark unterschiedlichen geographischen Regionen untersucht. Außerdem werden zwei Sätze von Satellitenorbits, polar und polnahe Orbits, analysiert.

Die Ergebnisse zeigen, dass das neue Wind-Retrieval die Fähigkeit hat die l.o.s. Windgeschwindigkeit in einem Höhenbereich von etwa 15 bis 35 km abzuleiten, wobei dies auch mit hochvariablen Windprofilen und hohen Windgeschwindigkeiten funktioniert.